MESOSCALE FRACTURE FABRIC AND PALEOSTRESS ALONG THE SAN ANDREAS FAULT AT SAFOD

A Thesis

by

RAFAEL ALMEIDA

Submitted to the Office of Graduate Studies of
Texas A&M University
in partial fulfillment of the requirements for the degree of

MASTER OF SCIENCE

December 2007

Major Subject: Geology

MESOSCALE FRACTURE FABRIC AND PALEOSTRESS ALONG THE SAN ANDREAS FAULT AT SAFOD

A Thesis

by

RAFAEL ALMEIDA

Submitted to the Office of Graduate Studies of
Texas A&M University
in partial fulfillment of the requirements for the degree of

MASTER OF SCIENCE

Approved by:

Chair of Committee, Judith Chester
Committee Members, Frederick Chester
David Schechter
Head of Department, John Spang

December 2007

Major Subject: Geology

ABSTRACT

Mesoscale Fracture Fabric and Paleostress along the San Andreas Fault.

at SAFOD. (December 2007)

Rafael Almeida, B.S. Universidad de Los Andes – Venezuela

Chair of Advisory Committee: Dr. Judith Chester

Spot cores from Phase 1 drilling of the main borehole at the San Andreas Fault Observatory at Depth (SAFOD) were mapped to characterize the mesoscale structure and infer paleostress at depth. Cores were oriented by comparing mapped structures with image logs of the borehole. The upper core (1476-1484 m measured depth, MD) is a medium-grained, weakly foliated, hornblende-biotite granodiorite containing leucocratic phenocrysts and lenses. Principal structures are sub-vertical veins, shallow dipping shears, and natural fractures of unknown kinematics. The features are compatible with horizontal extension and right-lateral, normal, oblique-slip on faults striking approximately parallel to the SAF. The lower core (3055.6-3067.2 m MD) has massive-bedded, pebble conglomerates and coarse to fine grained arkosic sandstones grade into siltstones. Principal structure features are conjugate shears and two minor faults. The fracture fabric is consistent with strike-slip faulting and a maximum principal compressive paleostress at ~80˚ to the SAF plane. This paleostress is essentially parallel to the current in situ stress measured in the main borehole and to paleostresses inferred from fracture fabrics in exhumed faults of the San Andreas system to the south. The similarity between the current state of stress and paleostress states supports the

suggestion that the maximum principal compressive stress direction is, on average, at high angles to the SAF and that the fault has been weak over geologic time.

ACKNOWLEDGMENTS

I would like to thank the many people who have contributed to my time here at Texas A&M. First of all I would like to thank my committee chair, Dr. Judith Chester. She has been very supportive throughout this project; her door has always been open for anything I might need, thank you professor. I would also like to thank my committee members, Dr. Frederick Chester for his continuous academic input throughout the project and Dr. David Schechter for his help and availability. I would also like to acknowledge Dr. Ray Guillemete; his patience and dedication are exemplary.

I would like to thank my officemates and friends, Isaac and Fernando, their support and friendship was invaluable in moments of doubt, of which there were many! I have made many good friends in College Station. They are Sergio, Pablo, Martin, Tosin, Pablo C., Ezequiel, and many more, thanks for the good times!

I would like to thank my family for their unwavering support, not only during my time at Texas A&M University, but always.

Finally, I'd like to thank my girlfriend Joanna. You're smile can brighten up even the grayest day, thank you for everything. I feel fortunate to be with such a special person.

TABLE OF CONTENTS

Page

1. INTRODUCTION

The mechanical behavior of large displacement mature faults has been controversial, with debates centering on the strength of large faults, such as the San Andreas Fault (SAF) in California [*Zoback et al., 1987*]. The strength of a seismic fault can be defined by the ratio of the stress drop to the total strength of the fault. If the stress drop is a small fraction of the fault strength, then the fault is considered strong; if the stress drop represents a large fraction of the fault strength, then the fault is considered weak [*Kanamori, 1994*]. Mechanically, the strength of a fault is often described in terms of the average, apparent, coefficient of sliding friction, which is given by the ratio of shear stress to normal stress. A strong fault is one defined by an average coefficient of friction of approximately 0.7; a weak fault by an average of about 0.1 [*Kanamori, 1994*].

Study of the SAF has revealed a fundamental paradox regarding the level of shear stress required to cause motion along a major plate boundary [*Brune et al., 1969*; *Hickman, 1991*]. This paradox, referred to as the "stress-heat flow paradox", stems from the fact that heat flow measurements have detected little or no evidence of frictionally generated heat, implying that this fault has slipped at low values of shear stress, and therefore is weak relative to the surrounding crust [*Zoback et al., 1987*]. Estimated values of shear stress are on the order of stress drops that occur during seismic events [*Kanamori, 1994*] and are much lower than the total stress predicted from laboratory-determined rock-friction strengths [*Byerlee, 1978*; *Hickman, 1991*]. Also the fact that the inferred regional maximum compressive stress is almost normal to the fault supports the hypothesis that the SAF slips at a low apparent coefficient of friction and is weak in an absolute sense (i.e. small shear stress components acts on fault) [*Hickman et al., 1994*].

This thesis follows the style of *Journal of Geophysical Research.*

An alternative hypothesis is that the fault is strong, consistent with typical laboratory rock friction data [*Byerlee, 1978*], and obeys Anderson-Byerlee mechanics, i.e., Mohr-Coulomb failure criterion with a high effective friction coefficient [*Scholz, 2000*]. This hypothesis states that the stress state directly adjacent to the fault is different from the far filed stress described above and is consistent with higher shear stresses. *Scholz* [*2000*] and *Scholz and Hanks* [*2004*] argue that many lines of evidence used to support the weak fault hypothesis are flawed. For example, they argue that the deformation features (e.g. fold axes) that indicate a near orthogonal relation between the maximum compressive stress and the SAF plane [*Mount and Suppe, 1987*] were compatible with wrench tectonics and a strong fault at the time they were formed [*Scholz, 2000*], but that these features were rotated by 20˚ to 30˚ since their formation [*Miller, 1998*]. With respect to the heat flow paradox, *Scholz and Hanks* [*2004*] propose that the observed regional heat flow is large and variable enough to hide or mask the frictional heat generated by a strong SAF. Furthermore, they propose that convective heat transfer processes, such as advection of circulating water throughout the fault zone, rather than conduction, can explain the apparent lack of a friction heat-flow anomaly.

The San Andreas Fault Observatory at Depth, SAFOD, is a broad project to drill into the hypocentral zone of repeating M~2 earthquakes on the SAF at ~ 3 km depth near Parkfield, California. One of the objectives of this project is to address the SAF stress-heat flow paradox [*Hickman et al., 2004*]. Two boreholes were drilled as part of SAFOD: (1) a vertical pilot hole which was completed during the summer of 2002 to a total depth of 2200 m. The borehole is 1.8 km southwest of the SAF surface trace and (2) a main borehole, which is adjacent to the pilot hole (7 m apart) at the surface that was drilled in

two phases. The first phase was completed during the summer of 2004 (Phase 1 of main hole) and the second phase was completed during the summer of 2005 (Phase 2 of main hole). The main borehole is vertical until 1500 m depth, where it deviates up to 60° from vertical and terminates at a total depth of ~3000 m. [*Boness and Zoback, 2006*].

During Phase 1 drilling of the main borehole, two approximately continuous, unoriented spot cores were taken on the northwest side of the SAF over the depth intervals from 1462-1469 m measured depth (MD), and 3056-3067 m MD. Over this cored interval the borehole orientation is 039°, 38°. Given the proximity of the spot cores to the surface trace of the SAF, these cores provide an excellent opportunity to characterize the deformation mechanisms, fracture fabric, and width of the damage zone on the western side of the fault at the southern end of the creeping segment, and provide the deepest, direct and independent estimate of the paleostress state adjacent to the fault. Through detailed mapping of the mesoscale features in the spot cores and comparison of these features to those imaged in the Formation Micro Imager (FMI) and Logging While Drilling-GeoVision Resistivity (LWD-GVR) borehole logs, we were able to orient the spot cores. Through an analysis of the orientation and distribution of the mesoscale fractures we were able to estimate the cumulative fracture fabric and paleostress state characteristic of the western margin of the fault near Parkfield, California. We find that the paleostress state determined from the fracture fabric is consistent with in situ stress measurements and high differential stresses inferred in the same borehole [*Boness and Zoback, 2004*], and with paleostress determinations made from exhumed faults of this system to the south [e.g., *Chester and Logan, 1987; Blenkinsop, 1990; Chester et al., 1993; Wilson et al., 2003*]. These data support a weak-fault-in-strong-crust-model [*Rice*

et al, 2005] for the SAF and suggest that the fault has been weak, on average, over geologic time.

1.1. Geology in the Vicinity of Parkfield, California

The SAFOD drill site is located in the Coast Ranges of central California, 1.8 km southwest of the SAF near Parkfield, California (Figure 1, all figures referred to in text are in Appendix 1) [*Hickman and Zoback, 2004*]. At this location the fault juxtaposes Salinian granitic basement on the southwest and Franciscan Complex on the northeast, as is the case along much of the fault in northern California, [*Simpson et al., 1988; Wentworth et al., 1992*]. The drill site is located at the extreme northern end of the rupture zone of the 1966, Magnitude (M) 6 Parkfield earthquake [*Hickman et al., 2004*]. It is situated on a relatively straight section of the SAF in central California. This segment forms the transition between the creeping segment of the SAF to the northwest [*Savage and Burford, 1971*] and the locked section that last ruptured in the M 8.3, 1857 Fort Tejon earthquake [*Sieh, 1978*], to the southeast [*Murray et al., 2001*]. Currently, geodetic and seismic data suggest that the southern section of the fault is locked (producing no movement or only small to moderate sized earthquakes). Most of the northern section of the fault also is currently locked with no detectable movement and few earthquakes since 1906 [*Harris and Segall, 1987*]. Between these locked sections, the SAF creeps at a rate of 40 mm/yr. From San Juan Bautista to Parkfield, the creeping section produces numerous small (mostly M=5 and smaller) earthquakes but no large ones [*Wallace, 1990*].

Moderate-size earthquakes have occurred on the Parkfield section of the SAF at fairly regular intervals, occurring in 1857, 1881, 1901, 1922, 1934, 1966 and 2004. Although little is known about the 1857, 1881 and 1901 earthquakes, available data suggests that all seven earthquakes were about M 6 and ruptured the SAF at Parkfield. The similarity of teleseismic, long-period seismic waveform shapes and amplitudes for the 1922, 1934 and 1966 earthquakes suggest that these earthquakes ruptured the same segment of the fault in a similar manner [*Bakun, 1988*]. Based on these and other data, *Bakun and Lindh* [*1985*] hypothesized that these earthquakes are characteristic in the sense that they repeatedly ruptured the same area on the fault in an earthquake of about M 6. The creep rate has been measured and has remained at about 40 mm/yr. *Waldhauser et al*. [*2004*] have imaged two sub-parallel, seismically active faults based on precise relative microearthquake locations. The northeasterly fault is interpreted to be the main trace of the SAF, and the fault located about 200 m to the southwest is a secondary trace referred to as the Southwest Trace of the SAF or Southwest Fracture Zone [*e.g., Hole et al., 2001; Rymer et al., 2004*].

Since completion of the main borehole in September of 3005, creep has deformed the casing in two places [*Hickman, pers. comm.., 2007*]. The greatest casing deformation has occurred over the depth interval of 3302.5-3313 m MD. This region is hypothesized to be the location of the main trace of the SAF. At the end of the Phase 1 drilling, a clay-rich fault zone was captured at 3067 m MD. It has been suggested that this fault may be the southwest trace [*Zoback, pers. comm., 2005*]. A low seismic velocity zone also has been identified that spans 3150-3415 m MD.

In the pilot and main boreholes, Tertiary age sediments overlie 110 MYO Salinian granodiorites on the west side of the SAF [*Kistler and Champion, 1986*]. These sediments were transported northward along the SAF from their original emplacement as part of the southern Sierra Nevada batholith. The Salinian block and overlying Tertiary and Plio-Quaternary rocks and sediments are relatively undeformed [*McPhee et al., 2004*]. Thermochronological studies on samples from the pilot hole recognized 3 main phases of exhumation and burial, 1) a phase of gradual exhumation of the Salinian intrusives in the late Cretaceous and early Tertiary; 2) reburial by 1–1.5 km during the early phases of SAF transform faulting in the mid-Tertiary; and 3) exhumation related to uplift of the regional Coast Ranges during the late Cenozoic [*Blythe et al., 2004*]. These data indicate that in spite of having a lateral transport of 160 km over the last 5 Myr [*e.g. Sims, 1993*], only 1 km of net vertical motion occurred during the last 60 Myr [*Blythe et al., 2004*].

In contrast to the Salinian block, the block on the northeast side of the SAF is complexly deformed. The northeastern block is composed of the Franciscan Complex, overlain by the Great Valley sequence and late Cenozoic cover. A band of intricate folding and faulting, about 5 km wide, borders the SAF and is interrupted by fault-bounded slivers of basement rock that are not part of the Franciscan Complex [*McPhee et al., 2004*].

New geologic mapping, combined with high-resolution seismic reflection and refraction profiling in the vicinity of the SAFOD borehole, indicates a structurally complex SAF zone that is at least 5 km wide, and that is dominated by faults oriented subparallel to the surface trace of the SAF [*Rymer et al., 2004; Thayer et al., 2004*].

Geophysical data suggest that the SAF zone is composed of at least two flower structures in the upper 3 km, with the main trace approximately centered on the more easterly of these structures. The SAFOD drill site is located near the center of the westernmost flower structure. The flower structures are interpreted to merge at or below 3 to 4 km depth [*Rymer et al., 2004*].

1.2 Fault Zone Studies

Many processes can contribute to the fabric and composition of fault-zone rocks. A mature fault zone with significant displacement probably reflects the cumulative deformation by thousands of earthquakes that could have occurred under varying stress conditions [*e.g., Sibson, 1989; Chester et al., 2005; Rice et al., 2005*]. Variations in stress state along the fault also can reflect the juxtaposition of fault irregularities [*e.g., Saucier et al., 1992; Chester and Fletcher, 1997; Chester and Chester, 2000*]. Other factors may also affect the deformation fabric, such as migration of the active fault strand, coeval processes that can produce different local stress states and interseismic processes that can change the strength and the structure of the fault [*Flinn, 1977; Robertson, 1982; King, 1983; Chester and Logan, 1986; Sibson, 1986; Dor et al., 2006b*].

Fault initiation and growth models have been developed primarily on the basis of field observation, experimental rock deformation studies and theoretical modeling. From these studies several models for brittle deformation in a fault zone have been developed, including the "Andersonian" model of faulting [*Anderson, 1951*], the "cohesive crack" model [*Cowie and Scholz, 1992*] and the "wear" model [*Scholz, 1987*].

The Andersonian model of faulting assumes a homogenous state of stress in the crust and Coulomb failure behavior. Faults are predicted to form at acute angles (~30˚) to the maximum principal compressive stress axis for most rock types [*Anderson, 1951; Scholz, 1990*]. Assuming homogeneous stress and Coulomb failure, microfracture fabrics should display a preferred orientation of fracture planes that parallel the maximum principal compressive stress that bisects mesoscopic shears [*Anderson, 1951; Scholz, 1990*].

The "cohesive crack" model [*Cowie and Scholz, 1992*] describes inelastic deformation that occurs at a crack tip in the "process" or "breakdown" zone of a fault [*Reches and Lockner, 1994; Cox and Scholz, 1988*]. As cracks in the process zone coalesce to form a surface of slip, the process zone and tip of the crack propagate. This model implies that most of the brittle deformation occurs early in the fault formation process. Alterations in the stress field in a propagating mode II crack will result in an asymmetric fabric, one in which the microfractures preferentially form at 20˚ and 70˚ to the fault on the compressional and extensional side of the fault, respectively [*Vermilye and Scholz, 1998*]. Assuming Coulomb-type failure in the process zone, the microfracture orientations should bisect mesoscale conjugate shear fractures. The cohesive crack model also is used to describe deformation in the vicinity of earthquake rupture tips. If so, then fracture fabrics in fault zones also could reflect repeated deformation from earthquake slip events throughout the life of the fault.

The "wear" models predict an increment in the deformation along the fault with increased displacement [*Scholz, 1987*; *Chester and Fletcher, 1997*]. Displacement along a rough fault surface produces local stress concentrations [*Saucier et al., 1992; Chester*

and Fletcher, 1997; Chester and Chester, 2000]. As slip continues, stress cycling will occur in the adjacent wall rocks. The assumption that increasingly larger irregularities are juxtaposed as displacement increments, leads to an outward extension of damage from the fault surface, shearing of asperities, and formation of cataclastite [*Scholz, 1987*]. The microfractures and mesoscale fracture fabric will record the damage that has occurred over the life of the fault and will record the average orientation of the stress in the deforming region along the fault [*e.g. Chester and Chester, 2000; Wilson et al., 2003*].

In the Punchbowl fault, an ancient strand of SAF, *Wilson et al.* [*2003*] found that the preferred orientation of microfractures varies with distance from the fault core. The orientation and timing of microfractures suggest that the average stress-state in the damage zone of the fault was similar throughout most of the faulting history and was most consistent with a fabric generated by stress cycling associated with slip on a geometrically irregular, relatively weak fault surface [*e.g. Chester and Fletcher, 1997; Chester and Chester, 2000*]. However, the microfracture fabric in the innermost damage zone and fault core also is consistent with the accumulation of wear associated with the passage of many earthquake ruptures, and the outermost portion of the damage zone may have recorded an early stage of fault-formation under a paleostress field consistent with Andersonian faulting [*Wilson et al., 2003*].

Recently *Dor et al.* [*2006a*] found that the intensity of fracturing along the San Jacinto, San Andreas and Punchbowl fault zones is asymmetric, which they suggest is compatible with crack tip stress states and preferred rupture propagation directions. The two-dimensional, plane-strain, finite-difference model of a dynamic rupture along an interface suggests a preferred propagation direction of earthquake ruptures along a fault

that separates media with different elastic properties [*Ben Zion and Andrews, 1998; Ben Zion, 2001, Ben Zion and Sammis, 2003; Brietzke and Ben Zion, 2006*]. The data of *Dor et al.* [*2006a*] are consistent with a preferred northwestward propagation direction for ruptures on all three faults. Outcrop observations indicate that damage favors the northeast side of the SAF, regardless of the rock type [*Dor et al., 2006a; Dor et al., 2006b*].

Models have been developed to estimate the patterns of off-fault secondary failure adjacent to large displacement faults associated with earthquake rupture [*Poliakov et al., 2002; Rice et al. 2005*]. These models consider variations in off-fault stress states as a function of rupture propagation velocity, breakdown zone length, residual strength, Poisson ratio, fault strength and Skemptons factor. The models predict shear and tensile failure distribution, depending on the variation of the modeled parameters. An important element of these models is that they compare cases where the regional maximum principal compressive stress is at a high angle versus a low angle to the main fault. This could be very useful when comparing mesoscopic and microscopic fracture patterns and trying to determine a viable mechanical model for the SAF.

Although numerous studies have used the preferred orientations of microfractures to infer paleostress directions at their time of formation [*e.g. Friedman, 1969; Gallagher, 1974; Lespinasse and Pecher, 1986; Laubach et al., 1989; Ren et al., 1989; Vollbrecht et al., 1999; Takeshita and Yagi, 2001*] as well as to correlate the mesoscale and microscale fracture fabrics [*e.g. Ortega and Marrett, 2000; Dezayes et al., 2000; Laubach, 2002*], few studies have investigated microfracture fabrics of seismic faults.

In a microfracture study on samples recovered from the Cajon Pass Scientific borehole located about 4 km northeast of the SAF, *Blenkinsop* [*1990*] noted two distinct sets of microfractures, each with a characteristic mineral fill, and clear cross-cutting relationships. *Blenkinsop and Sibson* [*1992*] interpreted the cracks to represent aseismic deformation, being devoid of crack-seal textures expected for multiple rupture events. Veins with euhedral grain fill suggest a slow crack growth (same rate as chemical reactions) and display little to no evidence of shear.

Seismic anisotropy observed in Vertical Seismic Profile studies in the same borehole did not correlate with the present stress state, but rather with the observed microfracture fabric [*Blenkinsop and Sibson, 1992*]. Contrary to this, the seismic anisotropy measured in the pilot hole at SAFOD, is consistent with the in-situ stress state determined from the borehole breakout analysis and has been interpreted to reflect the preferential closure of fractures in response to an anisotropic state of stress [*Boness and Zoback, 2004*].

Models have been developed to calculate the amount of heat that a continental strike-slip shear zone can produce [*Lachenbruch and Sass, 1980; Leloup et al., 1999*]. These models consider thermal and mechanical parameters such as thermal conductivity, brittle-ductile transition depth, basal heat flow, radioactive heat production in the crust, slip-rate, crust density, upper mantle density, the coefficient of friction in the crust and upper mantle friction coefficient. A fast slipping fault (e.g. velocity of 10 cm/yr) with a high friction coefficient (e.g. μ=0.6), affecting an initially cold lithosphere (e.g. with a basal heat flow of 10 mW/m^2 and a thermal conductivity of 2.5 W/mK) composed of hard crust and mantle would yield the maximum shear heating effect, with final

temperatures of 933°C at the, Moho (i.e., temperature increase of 587°C), and 743°C at 20 km (i.e., temperature increase of 474°C). This probably corresponds to the absolute maximum shear-heating effect that can be expected along large strike-slip faults [*Leloup et al, 1999*]. More efficient heat transport mechanisms, such as advection of hot fluids in the shear zone, have been called upon to explain differences between modeled results and observations in major strike slip faults [*Leloup et al, 1999*].

The possibility that the heat flow paradox can be explained by heat advection through groundwater flow in the vicinity of the SAF has been investigated through modeling [*Sass et al., 1997; Saffer et al., 2003; Fulton et al., 2004*]. Earlier models had evaluated the effects of topographically driven groundwater flow on heat flow near the SAF for a suite of fault strength and hydrogeological conditions [*Williams and Narisimhan, 1989*], but in the Parkfield area the results were inconclusive due to the large scatter of the data [*Saffer et al., 2003*]. *Fulton et al.* [*2004*] have corrected the thermal data from the Parkfield area for 3-D topographic effects that were responsible for most of the data scatter. The new modeling results show that for a strong fault, sufficient redistribution of heat by groundwater water flow is unlikely.

1.3 Borehole Geology and Geophysics

The main borehole at SAFOD penetrates sedimentary rock from the surface to approximately 770 m, and then granitic rocks to 1920 m where it intersects a fault contact with sedimentary rock, 230 m to the northeast from where the borehole deviates from vertical. The lower sedimentary sequence consists of alternating arkosic conglomerates,

sandstones and siltstones with intervals of finely laminated shale [*Boness and Zoback, 2006*].

Petrophysical logs were taken to characterize different properties of the lithologic units penetrated by the SAFOD main borehole. These include sonic velocity, resistivity, gamma ray, density and neutron porosity logs. The granitic section of the SAFOD main hole presents properties that are similar to the ones found in the SAFOD pilot hole [*Boness and Zoback 2004 and 2006*]. The main petrophysical characteristics of this section are: 1) Compressional and shear sonic velocities display an overall trend that increases with depth, but with intervals of lower velocities which may be associated with minor fractures [*Boness and Zoback, 2006*]; 2) The resistivity also presents an increasing trend with depth with values that range from 10 ohm-m in the Tertiary sediments to a maximum of 500 ohm-m in the granodiorite; 3) The natural gamma varies between 50 American Petroleum Institute units (API) to about 100 API in the granitic rocks, which has been interpreted to reflect changes in rock mineralogy [*Boness and Zoback, 2006*]; and 4) The density and neutron porosity logs coincide at about 10 % porosity, which is a high value for this type of rock and has been interpreted to reflect the presence of pervasive fracturing around the borehole [*Boness and Zoback, 2006*].

The main petrophysical characteristics of the sedimentary section are: 1) Sonic velocities which are slightly lower than those measured within the granitic section, showing an overall increase with depth; 2) The resistivity also increases with depth; 3) The gamma ray is very similar to the measurements within the granitic section, which has been interpreted to reflect the arkosic composition of the sandstones [*Boness and Zoback, 2006*]; and 4) Porosity values obtained from density logs are consistent throughout the

sedimentary section at about 10%. The neutron porosity presents greater variation with a range of values from 10%-40%. Relatively, within this sequence, the sandstone units are characterized by relatively high velocities and resistivity, low gamma ray, and slightly lower density and neutron porosity than the rest of the sedimentary section and the shale units are characterized by decreased velocities and resistivity, and an increased gamma and neutron porosity [*Boness and Zoback, 2006*]. The principal geologic observations from the SAFOD main borehole are condensed in Table 1 (all tables referred to in text are in Appendix 2).

2. SPOT CORE HANDLING AND MAPPING PROCEDURES

The spot cores from Phase 1 drilling are samples of the damage zone and host rock west of the main trace of the SAF. Although fractured and locally fragmented, almost complete recovery was obtained from the cored intervals of 1462-1470 m MD (4798-4822') and 3055.5 -3067 m MD (10025-10063') (Figure 2). The upper spot core, boxes 1-9, consists of crystalline rock, and the lower spot core, boxes 10-23, consists of sedimentary rocks. The interval cored during Phase 2, boxes 1-4, is composed of sedimentary rocks on the east side of the main trace of the SAF, and is taken from the base of the Phase 2 borehole. Only 50% recovery was realized during Phase 2 from 3990-3998 m MD (13090-13116‘) (Figure 2). Only Phase 1 cores are discussed herein.

2.1 Core Handling

The core was taken in intervals of 9.14 m with a hollow-circle diamond toothed drill bit and collected in a thick-wall aluminum sleeve. The Phase 1 spot cores have a diameter of 101.6 mm and the Phase 2 spot core has a diameter of 66 mm. The sandstone spot core from Phase 1 was taken out of the bottom of the 238 mm borehole casing, and the spot core from Phase 2 was taken out of the bottom of the 216 mm borehole casing.

Once on deck, the entire cored interval, including the core-catcher sample, was used to calculate the core length after pushing the rock pieces together and measuring to the nearest millimeter. The sleeves and core were cut into 0.9 m long sections (boxes), and the sleeves were split by cutting them down the axis (Figure 3). The contents were transferred into a split plastic liner for storage. Plastic spacers are used to separate

individual pieces and reconstructed groups of pieces in the core liner. These spacers may represent a substantial interval of no recovery. Each piece of the core is numbered sequentially from the top of each section, beginning with number 1; reconstructed groups of pieces are assigned the same number but are lettered consecutively. Pieces are labeled only on the outer cylindrical surfaces of the core. If a piece could be oriented with respect to up and down, an arrow was added to the label pointing to the top of the section. The core was then photographed in rails with ruler marks for reference [*Shipboard Scientific Party, 2001*]. The core and liners were shrink-wrapped in plastic to prevent rock pieces from vibrating out of sequence during transit from the wellsite to the Integrated Ocean Drilling Program Gulf Coast Repository at Texas A & M University, where it is housed in refrigerators.

2.2 Core Mapping

As expected, the integrity of the spot cores is fair in some places, making it difficult to handle the core without it falling apart. When the core was handled, latex gloves were used to prevent contamination with organic residues and distilled water was used sparingly to wet the core surface. After each section of core was mapped it was shrink-wrapped in plastic and returned to refrigerated storage.

Contiguous sections of core were defined by correlating and aligning features in adjacent boxes. Once the sections were aligned, the core was marked with a common black orientation line on the outer surface of the core; the black orientation line is parallel to the core axis. Both spot cores from Phase 1 could be pieced back together into 3 contiguous sections: 1) boxes 1-2, 3-6, 7-9 for the granodiorite core (Figure 4), and 2)

boxes 10-12, 13-17, 18-20 for the sedimentary rock core (Figure 4). Boxes 21-23 were too fractured to align. Because individual sections of core could have rotated about the core axis during recovery, the black orientation line is not continuous across uncorrelated boxes (Figure 6).

After alignment, wrap-around tracings were made of the outer surface of the core to produce 1:1 maps (Figures 4 and 5). This was done by wrapping a transparent polyfilm around each 0.9 m section of core. Mesoscale fractures, basic lithology, layering and foliations were traced on the polyfilm. Fractures that were filled or partially filled with mineral deposits or gouge were classified as natural fractures. Open fractures that contained no mineral fill or gouge were classified as open and possibly coring-induced fractures. Since the core was laid on a rail, the tracings were done one side at a time.

Planar fabric elements (e.g., fractures, bedding, and foliation) that cut the core appear as sinusoids on the wrap-around maps (Figures 4 and 5). We determined the orientations of the mesoscale quasi-planar structural features present in the maps by fitting these to sinusoids (Appendices A1 and A2). Each feature fit by a sinusoid is numbered and the respective orientation tabulated (Appendices A1 and A2). All orientations of planar features are determined from the amplitude and position of the sinusoids relative to the reference frame defined by the axis of the spot core and the black orientation line (Figure 6).

3. STRUCTURAL CHARACTERIZATION OF PHASE 1 GRANODIORITE SPOT CORE

3.1. Spot Core Description

The cored interval from 1462-1470 m consists of a medium-grained hornblende-biotite granodiorite with small leucocratic phenocrysts (1-3 mm in diameter) and thin lenses (up to several cm thick) that are weakly foliated in some places. Small shears, natural fractures, and veins that record both high- and low-temperature shear deformation are present in this cored interval. The dominant brittle deformation features are a series of sub-vertical fractures and moderately dipping shears, both of which contain some secondary mineral fill, and halos of low-grade alteration that discolors the granodiorite host.

Two general types of veins can be distinguished; one type is associated with thick alteration halos (up to 2 cm in width) that generally are salmon colored (e.g., at 4818' (1468.5 m MD), Figure 4). The vein filling in the first type has a light greenish color with thicknesses of up to several mm, although in some veinlets this filling is barely or not visible (they appear as a fine band of altered rock). The second type of vein displays no apparent alteration and the vein fill is darker (e.g., at 4815' (1467.6 m MD), Figure 4). Some smaller veins displayed in thin sections and in the interior of the core are arranged en echelon; this characteristic is not evident in the core walls, and therefore not illustrated in the core maps. The majority of mesoscopic veins are subparallel to the core axis.

The natural fractures are usually hairline fractures that occasionally show some evidence of shear offset; examples of several cross-cutting fractures occur at 4804'

(1464.3 m MD) (Figure 4). These do not present evidence of mineralization or alteration halos. As with the veinlets, microstructural study reveals the presence of many smaller fractures that are not recorded in the maps.

The foliation that is found in the core is defined by elongated, coarse-grained minerals (e.g., at 4818' (1468.5 m MD), Figure 4). The intensity of the foliation is variable, although in general it is localized to certain parts of the core. Towards the top of the core the foliation is better developed and characterized by smaller grain sizes and greater elongation of crystals (e.g., at 4799' (1462.7 m MD), Figure 4).

The leucocratic lenses vary greatly in size throughout the core, ranging from 1 cm (e.g., at 4798.5' (1462.5 m MD), Figure 4) to 15 cm in thickness (e.g., at 4809.5' (1465.5 m MD), Figure 4). They are mostly composed of coarse grained potassium-feldspar with lesser amounts of quartz. Sometimes there are small patches of granodiorite within the lenses (e.g., at 4807' (1465.2 m MD), Figure 4). The lenses are approximately subparallel to the foliation.

One of the more prominent structural features present in this spot core is a set of three prominent, shallow-dipping, shear zones (at 4802' (1463.6 m MD), 4805.5' (1464.7 m MD) and 4810' (1466.1 m MD), Figure 4). These zones are bordered by alteration halos very similar to those bordering the veins. They contain layers of gouge and greenish mineral fill with similar coloring as the halo-bordered veins of up to 1 cm in thickness. The host rock adjacent to these shear zones is not foliated. Two of the shear zones truncate leucocratic lenses (at 4805.5' (1464.7 m MD) and 4810' (1466.1 m MD), Figure 4).

The number of features present in each contiguous section of the spot core is small, not enough to define a preferred orientation for any specific fabric element for each of these sections (Figure 7).

3.2 Geographic Orientation

Each contiguous section of the core (boxes 1-2, 3-6, 7-9) was oriented relative to geographic North by comparing the wrap-around maps to the Formation Micro Imager (FMI) logs taken of the borehole wall (Figure 8). Specifically we compared sinusoids that were fit to planar features in the wrap-around maps to sinusoids that were fit to planar features evident in the image logs. Several details were taken into consideration when doing the comparison, including: 1) the difference in the diameter of the borehole (254 mm) relative to the diameter of the spot core (101.6 mm); 2) the differences in marked depths on the image logs as compared to the depths recorded on the outer-surface of the spot core, as the depths on the spot core do not factor in missing pieces and the image logs do not account for the stretch of the string that carries the imaging tool, both of which can contribute to depth uncertainties and; 3) the wrap-around maps are made looking towards the center of the cylinder, while the image logs are taken looking outward from the center.

The best correlation of features was achieved with the three prominent shear zones (4802’ (1463.6 m MD), 4805.5’ (1464.7 m MD) and 4810’ (1466.1 m MD), Figure 4) that intersect the core axis at a high angle. Additional correlations were based on other natural fractures and veins. The correlations allowed us to determine the true geographic orientation of the black orientation line (Figure 8 and Table 2), and with it, the true

orientation of the mapped features which are measured with respect to this black orientation line. The confidence in the geographic orientation of each contiguous section is variable, being greatest for boxes 1-2 and 3-6.

3.3 Combined Structural Fabric

The orientation data for all fabric elements are combined for the three contiguous sections and plotted relative to north (Figure 9). The data are plotted separately as: 1) igneous and metamorphic layering that includes the leucocratic lenses and foliation data, 2) shear fractures, 3) veins, and 4) natural fractures of unknown kinematics.

The poles to each type of planar fabric element having enough data (e.g., igneous and metamorphic layering, and natural fractures) are analyzed separately using data clustering statistics. Specifically, each dataset is compared to an ideal Fisher distribution in which the poles are randomly dispersed around a true orientation (i.e. the spherical equivalent of a Gaussian distribution) [*Fisher et al., 1987*]. The Fisher distribution model predicts that a certain proportion of a sample should occur inside a cone with an arbitrary half-angle, θ. We can test the suitability of the model by comparing this theoretical distribution with the distribution defined by the real data. The proportion of the sample that falls within the arbitrary half-angle, θ, can be plotted to facilitate a graphical comparison [*Priest, 1985*]. The mean vector of the real data, calculated and considered as the true orientation when performing the clustering analysis, and the 95% confidence cone (i.e., 95% confidence that true mean lies within the cone), were used in the analysis. The parameters that are used to establish preferred orientation are the normalized resultant vector (Rn) which measures the dispersion of the sample (closer to 1 means

preferentially oriented sample) and κ which is a measurement of randomness of the sample (0=random uniform distribution, as it gets higher the sample presents less random dispersion).

The orientation data for all fabric elements are corrected for the bias imposed by a linear survey (i.e. the borehole sampling bias). This type of sampling will tend to over-represent discontinuities that are sub-perpendicular to the borehole axis, and will under-represent discontinuities that are almost parallel to it [*e.g. Terzaghi, 1965; Hudson and Priest, 1983; Priest, 1985*]. To correct for this bias, the data are weighted by a factor *w*, defined by *Priest* [*1985*] as: $w = 1 / \cos \delta$, where δ is the angle between the pole to the discontinuity and the borehole axis.

The poles to the igneous and metamorphic layering (n=16) display a weak preferred orientation, and compare favorably to the Fisher distribution model, with Rn=0.74 and κ=3.58. The mean vector has an orientation of 58.4°, 312.9°, with a 95% confidence cone of 21.7°. That is, the layering dips moderately to the west, northwest (Figure 9).

The shear fractures and veins are too scarce to perform a meaningful statistical analysis of preferred orientation. The vein data, however, suggests approximately orthogonal, sub-vertical preferred orientation striking approximately 145° and 040°. The natural fractures with unknown kinematics are present in a sufficient quantity to allow cluster analysis. These features do not compare favorably to the Fisher model with Rn=0.68 and κ=3.03. The mean vector has an orientation of 82.2°, 012.3° with a 95% confidence cone of 17.2°.

Interpretation of the fabric analysis is greatly impacted by the weighting procedure and the presence of sub-vertical fractures. The probability of intersecting sub-vertical features with a vertical borehole is very low, and the procedure gives an infinite weighting value for the vertical fractures, which could completely skew all calculations. In order to avoid this, the weighting value was arbitrarily capped at 10 (Table 3) [*Priest, 1985*]. By maintaining a relatively high weighting value we are acknowledging that there is probably a high density of features with this orientation, and that they are not a random anomaly encountered in the borehole. The effect this has can be seen when we contour the natural fracture poles. Although the number of data points is not great enough to produce statistically significant contours, the data are contoured in order to qualitatively compare the difference between the weighted and unweighted fracture data sets (Figure 10). The unweighted contours form very weak concentrations, while the weighted data set tend to have more defined maximas around the subvertical features. It is worth noting that even though there is no kinematic data for these natural fractures, their distribution does not preclude a possible conjugate fracture set origin. It is also worth noting that the three shear zones present in the spot core have an orientation that is sub-parallel to the SAF in this location.

4. STRUCTURAL CHARACTERIZATION OF SEDIMENTARY SPOT CORE

4.1 Spot Core Description

The upper portion (3055 – 3062 m MD) of the spot core through the sedimentary section is composed of pebble conglomerate to coarse-grained arkosic sandstone with lithic fragments of granite, sandstone, siltstone, and volcanic clasts (Figure 5). The beds are massive, well-cemented, and contain rare cobble-sized clasts. The lower portion (3062 – 3067 m MD) of the spot core is a fine-grained, well-cemented arkosic sandstone that grades down hole into a fine- to very fine-grained siltstone. Bedding is indistinct throughout most of this section, although one bedding surface is well-defined at 10053.5' (3064.3 m MD) (Figure 5), between the very fine sandstone and siltstone [*Almeida et al., 2005*]. The age of the unit is unknown; however, preliminary zircon fission track dating suggests a likely Paleocene or younger age [*Kirschner et al., 2007*].

The dominant brittle features In the upper spot core include: a) Irregular, somewhat diffuse cataclastic bands that are up to two cm thick and are oriented at high angles to the core axis (e.g., at 10037.5' (3059.5 m MD), Figure 5). These bands antecede the shear fractures as they are offset by them; b) Thinner, dark colored natural fractures that are up to several mm thick. These fractures are common in the pebble conglomerate and very coarse sandstone, and display consistent kinematic indicators and preferred orientations (e.g., at 10035.7' (3059 m MD), Figure 5); c) Mutually cross-cutting shear fractures, which seem to be the youngest feature based on cross cutting relationships (e.g., at depths of 10045' (3061.7 m MD) and 10052' (3063.8 m MD), Figure 5); d) Coring induced fractures which are usually normal to the borehole axis (disking) (e.g., at

10028.2’ (3056.6 m MD), Figure 5); e) Minor faults which show clear gouge development and juxtaposition of different rock types; two of these faults likely have displacements of at least several meters.

The first of the two minor faults is located at 3062 m MD (10047.7’, Figure 5), is a cataclastic zone that juxtaposes coarse-grained sandstone and a very fine-grained siltstone; this is the largest cataclastic zone captured in the core. The other large fault is at the very base of the spot core at 3067 m MD (10067’, Figure 5). It also juxtaposes different lithologies, siltstone against sandstone, and has been hypothesized to be the Southwest Trace of the SAF [*Zoback, pers. comm.., 2006*]. An increase in damage towards this fault can be observed within the siltstone, and the fault consists of two of gouge layers containing a sliver of fractured rock. The 3067 m MD fault is oriented at about 22˚ to the core axis. The slip direction is approximately parallel to the direction of maximum inclination of slip plane relative to the core axis.

The fractures throughout the core form conjugate sets that appear to have a preferred orientation within each contiguous section (Figure 5). The contraction direction of the conjugate sets appears to be sub-parallel to the core axis throughout the three sections. The poles to the shear fractures, when plotted with respect to the black orientation line, define two point concentrations in each of the three contiguous core sections (Figure 11). On the basis of the relative number of fractures and the inclination of the fractures relative to the borehole axis, we define a dominant set (set A) and a secondary set (set B) in each of the 3 contiguous sections, boxes 13-17 (n_a=46 and n_b=26, Figure 11b), 18-20 (n_a=19 and n_b=4, Figure 11c), and 10-12 (n_a=12 and n_b=2, Figure 11a). Based on the 95% confidence cone, the strongest preferred orientation is present in

Boxes 13-17 (Figure 11b), followed by Boxes 18-20 (Figure 11c), and the weakest preferred orientation is present in Boxes 10-12 (Figure 11a).

4.2 Fracture Fabric and Alignment of Contiguous Sections

Given the overall similarity in the fracture fabric between and consistent kinematics, the three contiguous sections of the sedimentary spot core (Figure 11), we assume that these fractures are related and the fabrics can be used to align the three sections of core to each other. Accordingly, each section of core was rotated around the borehole axis to achieve the best fabric correlation. In order to determine the amount of rotation required for aligning the contiguous sections of core, two steps were taken: 1) The angle between the mean vectors of each equivalent fracture set was determined. This yielded two different angles, one between the means of the two set A's and another between the means of the two set B's (Table 4); 2) The two angles were then averaged taking into account the number of data points in each corresponding set, given by:

$$avg_{weighted} = \{[angle_{a1\text{-}b1} * (n_{a1} + n_{b1})] + [angle_{a2\text{-}b2} * (n_{a2} + n_{b2})]\} / (n_{a1} + n_{b1} + n_{a2} + n_{b2})$$

This correlation yielded an angle of rotation of 67.2° between boxes 10-12 and 18-20, and 86.1° between boxes 13-17 and 18-20. The poles to the fractures were then rotated by these angles about the borehole axis, to align the entire sedimentary section of core into the reference frame of boxes 18-20. The combined data (n=109) display strong preferred orientations with well-defined mean vectors. Once aligned, the combined data were analyzed in terms of the clustering of the data using the same procedure previously described for the granodiorite core (see page 23). The initial analysis confirms two

subsets exist within the fracture population. Each subset was analyzed individually (A: n=77, B: n=32) and demonstrated excellent correlation with the Fisher model (Table 5).

4.3 Geographic Orientation

Due to washouts in the borehole over the cored interval, the high resolution FMI logs were of poor quality and could not be used to correlate fractures imaged at the borehole wall to those traced on the outer surface of the spot core. Instead the core could be oriented to geographic North by correlating bedding imaged in the lower resolution Logging While Drilling-GeoVision Resistivity (LWD-GVR) logs to a bedding surface displayed in the spot core in Box 20 (Figure 5, Table 6). In order to compare the bedding attitudes, the pole to the bedding in the spot core was rotated about the borehole axis orientation (039°, 38°) to trace out a small circle that represents all possible pole orientations for the bedding plane (Figure 12). The possible pole orientations were compared to the mean vector determined from the five poles to the bedding measurements obtained from the LWD-GVR image logs over the same interval to determine the best fit for the bedding plane and to orient the core with respect to North. The best fit is achieved by a 195° clockwise rotation of the black orientation line about the core axis (039°, 38°). The shear fracture fabrics were then rotated in the same fashion to place them in geographic context. Table 7 shows the true orientation of the black orientation line in each contiguous section.

4.4 Fracture Kinematics

Observed kinematic indicators and cross-cutting relations suggest that the two fracture sets present in the spot core form a conjugate fracture set with best fit pole orientations of 129.6°, 38.8° and 279.6°, 51.2°. This geometry is consistent with strike-slip kinematics. The right lateral, synthetic set is better developed than the left lateral, antithetic set (Figure 13). The contraction direction for this conjugate set is more or less orthogonal to the SAF at this location. The bedding strikes sub-parallel to the SAF and dips slightly away from it, giving it an approximately orthogonal relation as well. The fractures are approximately normal to the bedding.

Figure 14 shows the orientations of the two minor faults cutting the spot core. The pole to the 3062 m MD fault is shown in red and coincides with other cataclastic faults cutting the core that form part of the dominant right-lateral set of shear fractures. The 3067 m MD fault, the one hypothesized to be the Southwest Trace of the SAF, was captured in the core catcher and so it is not possible to orient it by piecing it back together with the rest of the core. Given the inclination of the 3067 m MD fault relative to the core axis, we can plot all possible orientations of the pole to this fault, which trace out a small circle about the borehole axis (Figure 14). Based on these possible orientations, the 3067 m MD fault cannot be coplanar with the SAF. Recall that the slip vector for this fault is approximately parallel to the direction of maximum inclination to the core axis. Thus, if the fault strikes sub-parallel with the SAF, then it would have dip-slip kinematics, and if it strikes obliquely, then it has a strike-slip component. The absence of other dip-slip oriented fractures supports the interpretation that the 3067 m MD fault is a member of either the right-lateral or left-lateral, strike-slip faults defined by the rest of the fractures.

5. DISCUSSION

5.1 Paleostress Analysis of Granodiorite Structural Fabric

Some of the fracture planes found in the upper granodiorite spot core presented evidence of slip, with slip lineations being measured on five of them (Figure 14, Table 8). In all the fracture lineations measured, the slip vector displays a normal dip-slip and right-lateral strike-slip displacement. Normal-slip shears in conjunction with the existence of several subvertical, opening-mode fractures (veins) suggest horizontal extensional strain and a subvertical maximum principal compressive stress.

The veins are in a variety of orientations, but generally are sub-vertical consistent with more than one direction of horizontal extension. Based on the summary fabric plot (Figure 8) and the kinematic data (Figure 14 and Table 8), we interpret that the three major, shallow dipping shears (at 4802', 4805.5' and 4810', Figure 3) are normal, right-lateral, oblique-slip faults that strike sub-parallel to the SAF. The displacement on the three shears is incompatible with the expected right-lateral shear under fault-normal-contraction based on the current North American and Pacific Plate motions along the SAF. In the core, the long subvertical veins are either truncated by these shears or change from being vertical to being inclined, and intersect the outer surface of the core. Even though the subvertical veins display primarily opening-mode kinematics, they do show some evidence of some shear displacement. The shear-sense on the veins is similar to that on the three major, shallow dipping shear zones. Thus we interpret that these sub-vertical veins were reactivated in shear during the formation of the shallower dipping shear zones (Figure 15). The similarity in alteration halos and mineral fillings in both the veins and

the shallow dipping shear zones is consistent with concurrent activity. On the basis of the fracture kinematic data, we hypothesize that all of these features predate the more recent paleostress field responsible for the development and displacement along the of the San Andreas transcurrent system.

5.2 Paleostress Analysis of Sedimentary Structural Fabric

For the sedimentary section that is much closer to the surface trace of the SAF (Figure 2), we infer paleostress from the fracture fabric, assuming the Andersonian fault model that is based on Coulomb failure criterion. The Coulomb criterion predicts two oppositly dipping failure surfaces at approximately 30° to the maximum principal compressive stress and the line of intersection of these planes is parallel to the intermediate principal stress direction [*Anderson, 1951*]. Based on this model we can define the orientation of the three principal compressive stresses: σ_1 = 23.3°, 032.8°, σ_2 = 65.9°, 228.4° and σ_3 = 05.7°, 125.3°. The plane bisecting (035.3°, 84.2° SE) the conjugate set is 82.6° from the SAF (132°, 83° SW) at this locality. The principal compressive stresses are essentially parallel and perpendicular to bedding, approximately horizontal and vertical, and consistent with right-lateral strike-slip on the SAF (Figure 16).

The apparent large dihedral angle (>95°) of the conjugate fracture set is can be interpreted in several ways. One possibility is that the dihedral angle was originally closer to 60° at the time the conjugate set formed, and then widened as the fracture planes rotated with increasing strain (i.e.,. due to pure shear of the sediments during faulting). Another possibility is that the present orientations are the same as when the shear

fractures were formed. In this latter case the fabric could indicate compactive cataclastic flow deformation at an elevated mean compressive stress where compactive shear bands form at large angles to σ_1 [*Wong, 1990; Wong et al., 1997; Wong et al., 2001; Challa and Issen, 2004*]. The response of a porous rock to compressive stress will depend greatly on the grain size, porosity and amount of cementation. For a coarse grained, porous, poorly-cemented sedimentary rock, compressive loading tends to create stress concentrations at contacts between grains, which can lead to consolidation by the crushing of the grains [*Gallagher et al., 1974*] and the development of compactive shear bands [*e.g. Wong, 1990*]. Another possibility could be the existence of preexisting orthogonal joint sets that were later reactivated as shear fractures.

The fracture fabric of the sedimentary section (Figure 13), sampled by the lower spot core taken at SAFOD, is similar to fracture fabrics in the damage zones of exhumed faults of the SAF system to the south (e.g., Punchbowl and San Gabriel faults). The Punchbowl and San Gabriel Faults are inactive strands of the SAF that have been exhumed approximately 2-4 km [*Anderson et al, 1983; Chester and Logan, 1986; Chester et al., 1993*]. This makes them excellent analogs for comparison with the data presented herein. In both exhumed fault zones the fracture fabrics in the damage zone of the faults are characterized by a set of conjugate, strike-slip subsidiary faults. Inversion of the subsidiary fault data obtained from the crystalline rocks on both sides of the North Branch San Gabriel fault yields a maximum principal compressive stress that is oriented at 60°-80° to the San Gabriel fault [*Chester et al., 1993*].

The Punchbowl fault juxtaposes the San Gabriel Basement Complex and the Punchbowl Formation at Devil's Punchbowl County Park. The latter formation is very

similar to the lithology intercepted in the lower, Phase 1 spot core, consisting of cobbly to pebbly arkosic sandstone with interbedded siltstone [*Woodburne, 1975, Chester and Logan, 1986; Chester and Chester, 1998*]. The subsidiary faults in the damage zone of the Punchbowl fault display somewhat different orientations on each side of the fault, possibly reflecting the different lithologies and magnitude of deformation. Nevertheless, the fractures on both sides of the fault define a conjugate set that indicates a maximum principal compressive stress that is almost normal to the Punchbowl fault [*Chester and Logan, 1987*]. The dihedral angle in the Punchbowl Formation is greater that 60° [*Chester and Logan, 1986; Wilson et al., 2003*].

The paleostress state during Punchbowl faulting also was interpreted from microfracture orientations by *Wilson et al.* [*2003*]. In their study, microfracture orientations in samples of the outer and inner damage zones both suggest that the maximum principal compressive stress was approximately normal to the Punchbowl fault throughout its history.

The paleostress state estimated from the fracture orientations in the sedimentary section, sampled by the lower, Phase 1 spot core also can be compared to in situ stress estimates along the SAF. Estimates of in-situ stress in the SAFOD pilot hole (1.8 km from the SAF), based on borehole breakouts and tensile cracks, suggest that the maximum principal compressive stress rotates with depth from 25° ± 10° to the SAF at 1000–1150 m, to 69° ± 14° to the SAF at 2050–2200 m. The angle between the maximum principal compressive stress and the SAF at depths of 2050–2200 m in the pilot hole is similar to that observed in central California at even greater distances from the SAF [e.g., *Hickman and Zoback, 2004; Townend and Zoback, 2004*]. This similarity

could mean that this stress state represents the far-field stress state rather than that in the actively shearing portion of the fault zone.

In-situ stress orientations also have been measured in the main borehole at SAFOD using the fast direction of the shear wave anisotropy [*Boness and Zoback, 2006*]. Here, the angle between the maximum principal compressive stress axis and the SAF gradually changes with increasing depth and decreasing distance to the fault (Figure 2). At the location of the sedimentary rock spot core, (~2500 m vertical depth), the maximum horizontal stress is estimated to be ~70˚ to the SAF [*Boness and Zoback, 2006*], consistent with the paleostress orientation obtained from the spot core (Figure 17). The in situ stress measurement from the base of the Phase 1 borehole is the closest estimate of in situ stress made at depth at this location, being less than 150 m from the SAF [i.e., from the site of maximum borehole deformation].

The results obtained from this study also can be compared with the data obtained from the Cajon Pass borehole, which was drilled approximately 4 km NE of the SAF, on the southwest edge of the Mojave Desert [*Zoback et al., 1988*]. In-situ maximum horizontal compressive stress measurements made from borehole breakouts at this site have an average orientation of 057°±19°, which indicates nearly fault-normal compression with a small component of left-lateral shear on planes parallel to the SAF [*Shamir and Zoback, 1992*]. Although fault-normal compression is similar to the state of stress estimated elsewhere along the SAF, the left-lateral component of shear is in clear contrast to kinematic measurements made elsewhere that indicate overall right-lateral shear on the SAF [*Mount and Suppe, 1987; Wallace, 1990*]. These observations have been explained by the accumulation of residual stresses along the fault due to undulations

in the fault surface [*Saucier et al., 1992*]. Another likely explanation may be that the data from Cajon Pass reflect the overprint of the regional stress field by the local stress field produced by the Squaw Peak thrust system which is located less than 1 km away from the borehole [*Blenkinsop, 1990, Mesiling and Weldon, 1989*]. Microfractures observed in core from the Cajon Pass borehole display preferred orientations, and although the timing of these is not well-constrained. It is important to note that one set of microfractures is perpendicular to the SAF [*Blenkinsop, 1990; Wang and Sun, 1990; Blenkinsop and Sibson, 1992, Wilson et al. 2003*].

The far-field stress state has been studied extensively all along the SAF. One of the main indicators of regional fault-normal compression is the existence of abundant fold axes that are oriented parallel to the SAF. *Mount and Suppe* [*1987*] studied a subset of these folds in central California, concluding that the folds formed in this fault-parallel orientation and were not rotated into parallelism by shearing, as classical wrench tectonics would suggest [*Wilcox et al., 1973*]. Borehole breakout measurements also have been made throughout California and corroborate the inferences of stress using fold axis data [*Zoback et al., 1987; Mount and Suppe, 1987; Townend and Zoback, 2004*]. Additional attempts to determine the far-field state of stress along the SAF are based on the orientation of clastic dikes and sills [*Boehm and Moore, 2002*], modeling fold geometries [*Fiore et al., 2007*], seismic reflection data [*Wentworth and Zoback, 1989; Bloch et al., 1993*] and other data. All of these methods have been consistent in showing a long term fault-normal compression. Here we can investigate how this far-field stress state compares to the inferred stress state within 150 m of the actively shearing portion of the SAF.

Host rock adjacent to a fault experiences stress changes associated with movement past asperities [*e.g., Saucier et al., 1992; Chester and Fletcher, 1997; Chester and Chester, 2002*] and in response to the earthquake loading cycle [*e.g., Sibson, 1989; Chester et al., 2005; Rice et al., 2005*]. Due to the progressive accumulation of fracture damage during faulting, we can consider the paleostress orientations inferred from the fracture fabric in the lower, Phase 1 SAFOD spot core as a record of the average, long-term state of stress along the fault. Previous studies of microfractures along the Punchbowl fault indicate several episodes of fracturing over the life of the fault with similar fabrics for each episode [*Wilson et al., 2003*]. These data imply that the paleostress state inferred from the fracture fabric can be considered a record of the average temporal and spatial state of stress in the fault zone at seismogenic depths. Also, field studies in the northern Salinian block have shown that the inferred contractional strain field is approximately normal to the adjacent SAF and appears to have been consistently oriented in this direction during deformation events recorded over the past 30–45 MY [*Tavarnelli and Holdsworth, 1999*].

The similarity of present day stress orientations [*Boness and Zoback, 2004 and 2006*] with the paleostress orientations determined herein for the historically active SAF and for ancient traces of the SAF, such as the Punchbowl fault (active from ~1-5 Myr) and the North Branch of the San Gabriel Fault (active from ~13-5 Myr) [*Powell and Weldon, 1992, Chester et al., 1993*], leads us to suggest that fault-normal, maximum principal compressive stress is a general condition for the SAF at several km depth. Moreover, this fault-normal compression state of stress apparently exists up to distances within tens of m of the active zones. This implies that if stress rotations occur, as

described by *Rice* [*1992*], they must be confined to zones less than tens of m thick. These results combined with evidence for high deviatoric stresses in the crust adjacent to the SAF [*Mount and Suppe, 1987; Healy and Zoback, 1988; Lachenbruch and McGarr, 1990; Zoback and Healy, 1991; Boness and Zoback, 2006*] are consistent with a weak SAF/strong crust model [e.g., *Rice et al., 2005*], where the SAF has a lower coefficient of friction than that predicted by Byerlee's Law (0.6-0.9) [*Byerlee, 1978*], and the adjacent crust supports a high differential stress consistent with Byerles's law (~100 MPa) [*Hickman, 1991*].

6. CONCLUSIONS

- The granodiorite core taken from a depth of 1476-1484 m MD and a distance of 1.8 km from the San Andreas Fault, displays low angle shear zones that strike sub-parallel to the San Andreas Fault and that truncate sub-vertical veins. Both the veins and shear zones record normal, right-lateral, oblique slip kinematics.
- The granodiorite spot core, which likely samples rocks from outside the damage zone of the San Andreas Fault, displays a fabric that was probably inherited from a horizontal extensional stress state that predated the fault-normal compression associated with the modern San Andreas Fault system.
- The sedimentary section cored at a depth of 3085-3096 m MD and a distance of ~150m from the SAF, displays quasi-conjugate mesoscale shear fractures consistent with right-lateral, strike-slip kinematics. The fracture fabrics of the sedimentary rock record a high mean paleostress with the maximum principal compressive paleostress oriented approximately 80° from the San Andreas Fault plane.
- The similarity between the estimate of the current in situ stress, based on shear wave anisotropy along the main borehole, and the paleostress state inferred from the sandstone fracture fabrics adjacent to the active San Andreas Fault, suggests that a nearly fault-normal compressive stress state represents a long-term average state, and supports the general applicability of the "weak fault in strong crust" model.

REFERENCES

Almeida, R., J. Chester, F. Chester, D. Kirschner, T. Waller and D. Moore (2005), Mesoscale structure and lithology of the SAFOD phase I and II core samples, *EOS Trans. AGU*, *86*(52), Fall Meeting Supplement, Abstract T21A-0454,.

Anderson, E.M. (1951), *THE DYNAMICS OF FAULTING AND DYKE FORMATION WITH APPLICATIONS TO BRITAIN*, 206 pp., Oliver and Boyd, Edinburgh, Scotland, United Kingdom.

Anderson, J, R. Osborne, and D. Palmer (1983), Cataclastic rocks of the San Gabriel Fault – an expression of deformation at deeper crustal levels in the San Andreas Fault Zone, *Tectonophysics*, *98*, 209-251.

Bakun,W. H. (1988), Historic seismicity of the Parkfield area. California geology. *California Division of Geology and Mines*. *41* (3), 61 - 62.

Bakun, W. H. and A. G. Lindh (1985), The Parkfield, California, earthquake prediction experiment, *Science*, *229*, 619 – 624.

Ben-Zion, Y. (2001), Dynamic rupture in recent models of earthquake faults*, Journal of Mechanics and Physics of Solids, 49,* 2209-2244.

Ben-Zion, Y. and D. Andrews (1998), Properties and implications of dynamic rupture along a material interface, *Bulletin of the Seismological Society of America, 88*, 1085-1094.

Ben-Zion, Y. and C. Sammis (2003), Characterization of fault zones, *Pure and Applied Geophysics, 160*, 677-715.

Blenkinsop, T. (1990), Correlation of paleotectonic fracture and microfracture orientations in cores with seismic anisotropy at the Cajon Pass drillhole, southern California, *Journal of Geophysical Research, 95* (B7), 11143-11150.

Blenkinsop, T.G. and R. Sibson (1992), Aseismic fracturing and cataclasis involving reaction softening within core material from the Cajon Pass drill hole, *Journal of Geophysical Research, 97*, 5135–5144.

Bloch, R., R. Von Huene, P. Hart and C. Wentworth (1993), Style and magnitude of tectonic shortening normal to the San Andreas Fault across Pyramid Hills and Kettleman Hills South Dome, California, *GSA Bulletin, 105* (4), 464–478.

Blythe, A., M. D'Allesio and R. Burgmann (2004), Constraining the exhumation and burial history of the SAFOD pilot hole with fission track and (U-Th)/He thermochronometry, *Geophysical Research Letters, 31*, L15S16, doi:10.10 29/200 3GL019407

Boehm, A. and J. Moore (2002), Fluidized sandstone intrusions as an indicator of paleostress orientation, Santa Cruz, California. *Geofluids , 2*, 147–161.

Boness, N and M. Zoback (2004), Stress-induced seismic velocity anisotropy and physical properties in the SAFOD pilot hole in Parkfield, CA. *Geophysical Research Letters, 31*, L15S17, doi:10.1029/2003GL019020.

Boness, N and M. Zoback (2006), A multi-scale study of the mechanisms controlling shear velocity anisotropy in the San Andreas Fault Observatory at Depth, *Geophysics, 71* (5), F131-F146.

Brietzke, G. and Y. Ben-Zion (2006), Examining tendencies of in-plane rupture to migrate to material interfaces, *Geophysical Journal International, 167* (2), 807-819.

Brune, J.N., T.L. Henyey, and R.F. Roy (1969), Heat flow, stress, and rate of slip along the San Andreas Fault, California, *Journal of Geophysical Research, 74*, 3821-3827.

Byerlee, J. (1978), Friction of rocks, *Pure and Applied Geophysics*, *116*, 615-626.

Challa, V. and K. Issen (2004), Conditions for compaction band formation in porous rock using a two-yield surface model, *Journal of Engineering Mechanics, 130* (9), 1089-1097.

Chester, F. and J. Chester (1998), Ultracataclasite structure and friction processes of the Punchbowl Fault, San Andreas system, California, *Tectonophysics*, *295*, 199-221.

Chester, F. and J. Chester (2000), Stress and deformation along wavy frictional faults, *Journal of Geophysical Research, 105*, 23421-23430.

Chester, F. and J. Logan (1986), Implications for mechanical properties of brittle faults from observations of the Punchbowl Fault zone, California, *Pure and Applied Geophysics, 124*, 79-106.

Chester, F. and J. Logan (1987), Composite planar fabric of gouge from the Punchbowl Fault, California, *Journal of Structural Geology, 9*, 621-634.

Chester, F., J. Evans and R. Biegel (1993), Internal structure and weakening mechanisms of the San Andreas Fault, *Journal of Geophysical Research, 98* (B1), 771-786.

Chester, J. and R. Fletcher (1997), Stress distribution and failure in anisotropic rock near a bend on a weak fault, *Journal of Geophysical Research, 102*, 693-708.

Chester, J., F. Chester and A. Kronenberg (2005), Fracture surface energy of the Punchbowl Fault, San Andreas system, *Nature, 437*, 133-136.

Cowie, P. and C. Scholz (1992), Physical explanation for the displacement-length relationships of faults using a post-yield fracture mechanics model, *Journal of Structural Geology, 14*, 1133-1148.

Cox, S. and C. Scholz (1988), Rupture initiation in shear fracture of rocks: an experimental study, *Journal of Geophysical Research, 93*, 3307-3320.

Dezayes, C., T. Villemin, and A. Pecher (2000), Microfracture pattern compared to core-scale fractures in the borehole of Soultz-sous-Forets Granite, Rhine Graben, France, *Journal of Structural Geology, 22*, 723-733.

Dor, O., T. Rockwell and Y. Ben Zion (2006a), Geological observations of damage asymmetry in the structure of the San Jacinto, San Andreas and Punchbowl Faults in Southern California: A possible indicator for preferred rupture propagation direction, *Pure and Applied Geophysics, 163*, 301-349.

Dor, O., Y. Ben-Zion, T. Rockwell and J. Brune (2006b), Pulverized rocks in the Mojave section of the San Andreas Fault zone, *Earth and Planetary Science Letters, 245*, 642–654.

Fiore, P., D. Pollard, W. Currin and D. Miner (2007), Mechanical and stratigraphic constraints on the evolution of faulting at Elk Hills, California, *AAPG Bulletin, 91* (3), 321–341.

Fisher, N., T. Lewis and B. Embleton (1987), *STATISTICAL ANALYSIS OF SPHERICAL DATA*, 329 pp., Cambridge University Press, New York.

Flinn, D. (1977), Transcurrent faults and associated cataclasis in Shetland, *Journal of the Geological Society*, *133* (3), 231-247.

Friedman, M. (1969), Structural analysis of fractures in cores from the Saticoy Field, Ventura County, California, *AAPG Bulletin, 53*, 367-389.

Fulton, P., D. Saffer, R. Harris and B. Bekins (2004), Re-evaluation of heat flow data near Parkfield, California: Evidence for a weak San Andreas Fault, *Geophysical Research Letters, 31*, L15S15, doi:10.1029/2003GL019378.

Gallagher, J., M. Friedman, J. Handin and G. Sowers (1974), Experimental studies relating to microfracture in sandstone, *Tectonophysics, 21*, 203-247.

Harris, R., and P. Segall (1987), Detection of a locked zone at depth on the Parkfield, California, segment of the San Andreas Fault, *Journal of Geophysical Research, 92*, 7945-7962.

Healy, J. and M. Zoback (1988), Hydraulic fracturing stress measurements in the Cajon Pass research well to 2 km depth, *Geophysical Research Letters, 15*, 1005-1009.

Hickman, S. (1991), Stress in the lithosphere and the strength of active faults, in *US National report to the International Union of Geodesy and Geophysics, 1987-1990*, Reviews of Geophysics Supplement, 759-775.

Hickman, S. and M. Zoback (2004), Stress orientations and magnitudes in the SAFOD pilot hole, *Geophysical Research Letters, 31*, L15S12, doi:10.1029/2004/GL020043.

Hickman, S., M. Zoback, L. Younker and W. Ellsworth (1994), Deep scientific drilling in the San Andreas Fault zone, *EOS Transactions, 75* (12), 137.

Hickman, S, M. Zoback and W. Ellsworth (2004), Introduction to special section: Preparing for the San Andreas Fault Observatory at Depth, *Geophysical Research Letters, 31*, L12S01, doi:10.1029/2004GL020688.

Hole, J., R. Catchings, K. St. Clair, M. Rymer, D. Okaya and B. Carney (2001), Steep-dip seismic imaging of the shallow San Andreas Fault near Parkfield, *Science, 294*, 1513-1515.

Hudson, J. and S. Priest (1983), Discontinuity frequency in rock masses, *International Journal of Rock Mechanics and Mining Sciences, 20* (2), 73-89.

Kanamori, H. (1994), Mechanics of earthquakes, *Annual Revision in Earth and Planetary Sciences, 22*, 207-237.

King, G. (1983), The accommodation of large strains in the upper lithosphere of the earth and other solids by self-similar fault systems: The geometrical origin of b-value, *Pure and Applied Geophysics, 121*, 762-815,

Kirschner, D., J. Solum, J. Chester, S. Hickman, J. Garver and J. Evans (2007), Results of elemental, stable isotope, organic matter, and fission track analysis of SAFOD drill-hole cuttings and core material. *Earthscope National Meeting*.

Kistler, R. and D. Champion (1986), Rb-Sr whole-rock and mineral ages, K-Ar, 40Ar/39Ar, and U-Pb mineral ages, and strontium, lead, neodymium, and oxygen isotopic compositions for granitic rocks from the Salinian composite terrane, *Open File Report 01-453*, 84 pp., U.S. Geological Survey, Denver, USA.

Lachenbruch, A. and A. McGarr (1990), Stress and heat flow, in the San Andreas Fault system, California, *Professional. Paper 1515*, 261–277, U.S. Geological Survey.

Lachenbruch, A. and J. Sass (1980), Heat flow and energetics of the San Andreas Fault zone, *Journal of Geophysical Research, 85*, 6185–6223.

Laubach, S. (1989), Paleostress directions from the preferred orientation of closed microfractures (fluid-inclusion planes) in sandstone, East Texas basin, U.S.A., *Journal of Structural Geology, 11*, 603-611.

Laubach, S., R. Reed, J. Gale, O. Ortega and E. Doherty (2002), Fracture characterization based on microfracture surrogates, Pottsville Sandstone, Black Warrior basin, Alabama, *GCACS Transactions, 52*, 585-596.

Leloup, P., Y. Ricard, J. Battaglia and R. Lacassin (1999), Shear heating in continental strike-slip shear zones: model and field examples, *Geophysical Journal International, 136*, 19-40.

Lespinasse, M. and A. Pecher (1986), Microfracturing and regional stress field: A study of the preferred orientations of fluid inclusion planes in a granite from the Massif Central, France, *Journal of Structural Geology, 8*, 169-180.

McPhee, D., R. Jachens and C. Wentworth (2004), Crustal structure across the San Andreas Fault at the SAFOD site from potential field and geologic studies, *Geophysical Research Letters, 31*, L12S03, doi:10.1029/2003GL019363.

Meisling, K. and R. Weldon (1989), Late Cenozoic tectonics of the northwestern San Bernardino Mountains, Southern California, *GSA Bulletin, 101*, 106-128.

Miller, D. (1998), Distributed shear, rotation and partitioned strain along the San Andreas Fault, central California, *Geology, 26*, 867-870.

Mount, V. and J. Suppe (1987), State of stress near the San Andreas Fault: Implications for wrench tectonics, *Geology, 115*, 1143-1146.

Murray, J., P. Segall, P. Cervelli, W. Prescott and J. Svarc (2001), Inversion of GPS data for spatially variable slip-rate on the San Andreas Fault near Parkfield, CA., *Geophysical Research Letters, 28*, 359-362.

Ortega, O and R. Marrett (2000), Prediction of macrofracture properties using microfracture information, Mesaverde Group sandstones, San Juan basin, New Mexico, *Journal of Structural Geology, 22,* 571-588.

Poliakov, A., R. Dmowska and J. Rice (2002), Dynamic shear rupture interactions with fault bends and off-axis secondary faulting, *Journal of Geophysical Research, 107* (B11), doi:10.1029/2001JB000572.

Powell, R. and R. Weldon (1992), Evolution of the San Andreas Fault, *Annual Reviews, 20*, 431-468.

Priest, S. (1985), *HEMISPHERICAL PROJECTION METHODS IN ROCK MECHANICS*, pp. 124, George Allen and Unwin, London.

Reches, Z. and D. Lockner (1994), Nucleation and growth of faults in brittle rocks, *Journal of Geophysical Research, 99*, 18159-18173.

Ren, X., B. Kowallis and M. Best (1989), Paleostress history of the Basin and Range Province in western Utah and eastern Nevada from healed microfracture orientations in granites, *Geology, 17*, 487-490.

Rice, J. (1992), Fault stress states, pore pressure distributions, and the weakness of the San Andreas Fault, in *Fault Mechanics and Transport Properties of Rocks*, Academic Press, New York.

Rice, J., C. Sammis and R. Parsons (2005), Off-fault secondary failure induced by a dynamic slip pulse, *Bulletin of the Seismological Society of America, 95*, 109-134.

Robertson, E. (1982), Continuous formation of gouge and breccia during fault displacement in *Issues in Rock Mechanics, Proceeds 23rd Symposium Rock Mechanics*, edited by R.E. Goodman and F.E. Heuse, American Institute of Metallurgy and Petroleum Engineering, New York.

Rymer, M. and R. Catchings, M. Thayer and J. Arrowsmith (2004), Structure of the San Andreas Fault zone and SAFOD drill site as revealed by surface geologic mapping and seismic profiling near Parkfield, *Eos Trans. AGU, 85*(47), Fall Meeting. Supplement, Abstract T11F-08

Saffer, D., B. Bekins and S. Hickman (2003), Topographically driven groundwater flow and the San Andreas heat flow paradox revisited, *Journal of Geophysical Research, 108* (B5), doi:10.1029/2002JB001849.

Sass, J., C. Williams, A. Lachenbruch, S. Galanis and F. Grubb (1997), Thermal regime of the San Andreas Fault near Parkfield, California, *Journal Geophysical Research, 102* (B12), 27575–27585.

Saucier, F., E. Humphreys and R. Weldon (1992), Stress near geometrically complex strike-slip faults: Application to the San Andreas Fault at Cajon pass, Southern California, *Journal of Geophysical Research, 97* (B4), 5081-5094.

Savage, J. C., and R. O. Burford (1971), Discussion of paper by C. H. Scholz and T. J. Fitch, "Strain accumulation along the San Andreas Fault", *Journal of Geophysical Research, 76*, 6469-6479.

Scholz, C. (1987), Wear and gouge formation in brittle faulting, *Geology, 15*, 493-495.

Scholz, C (1990), *The Mechanics of Earthquakes and Faulting*, Cambridge University Press, New York.

Scholz, C. (2000), Evidence for a strong San Andreas Fault, *Geology, 28*, 163-166.

Scholz, C. H., and T. C. Hanks (2004), The strength of the San Andreas Fault: A discussion, in *Rheology and Deformation of the Lithosphere at Continental Margins*, edited by G. D. Karner et al., Columbia University Press, New York.

Shamir, G. and M. Zoback (1992), Stress orientation profile to 3.5 km depth near the San Andreas Fault at Cajon Pass, California, *Journal of Geophysical Research, 97* (B4), 5059-5080.

Shipboard Scientific Party (2001), Leg 191 summary, in *Proceedings Of the Ocean Drilling Program, Initial Reports,* edited by T. Kanazawa et al., Ocean Drilling Program College Station, TX, 1-49.

Sibson, R. (1986), Brecciation processes in fault zones: Inferences from earthquake rupturing, *Pure and Applied Geophysics, 124* (1/2), 159-175.

Sibson, R. (1989), Earthquakes faulting as a structural process, *Journal of Structural Geology, 11* (1-2), 1-14.

Sieh, K. E. (1978), Slip along the San Andreas Fault associated with the great 1857 earthquake, *Bulletin of the Seismological Society of America, 68* (5), 1421-1448.

Simpson, R., R. Jachens and C. Wentworth (1988), Average topography, isostatic residual gravity, and aeromagnetic maps of the Parkfield region, California, *Open File Report 89-133*, U.S. Geological Survey, Denver, USA.

Sims, J. D. (1993), Chronology of displacement on the San Andreas Fault in central California: Evidence from reversed positions of exotic rock bodies near Parkfield, CA, in *The San Andreas Fault System: Displacement, Reconstruction, and Geologic Evolution*, GSA Memoir 178, 231-256, Denver.

Takeshita, T and K. Yagi (2001), Paleostress orientation from 3-D orientation distribution of microcracks in quartz from the Cretacous granodiorite core samples drilled through the Nojima Fault, south-west Japan, *The Island Arc, 10*, 495-505.

Tavarnelli, E. and R. Holdsworth (1999), How long do structures take to form in transpression zones? A cautionary tale from California, *Geology, 27* (12), 1063-1066.

Terzaghi, R.D. (1965), Sources of error in joint surveys, *Geothechnique, 15*, 287-304.

Thayer, M., J. Arrowsmith, J. Young, A. Fayon and M. Rymer (2004), Geologic structure of Middle Mountain within the San Andreas Fault zone near Parkfield, California. *Eos Trans. AGU, 85*(47), Fall Meeting Supplement, Abstract T13A-1335.

Townend, J. and M. Zoback (2004), Regional tectonic stress near the San Andreas Fault in central and southern California, *Geophysical Research Letters, 31*, L15S11, doi:10.1029/2003GL018918.

Vermilye, J. and C. Scholz (1998), The process zone: A microstructural view of fault growth, *Journal of Geophysical Research, 103*, 12223-12237.

Vollbrecht, A., M. Stipp and N. Olesen (1999), Crystallographic orientation of microcracks in quartz and inferred deformation processes: A study on gneisses from the German Continental deep Drilling Project (KTB), *Tectonophysics, 303*, 279-97.

Waldhauser, F., W. Ellsworth, D. Schaff and A. Cole (2004), Streaks, multiplets, and holes: High-resolution spatio-temporal behavior of Parkfield seismicity, *Geophysical Research Letters, 31*, L18608, doi:10.1029/ 2004GL020649.

Wallace, R. E. (1990), *The San Andreas Fault System, California: Prof. Paper 1515*, 283 pp., U. S. Geological Survey, Denver, USA.

Wang, C.-Y. And Y. Sun (1990), Oriented microfractures in Cajon Pass drill cores: Stress field near the San Andreas fault, *Journal of Geophysical Research, 9*, 11135–11142.

Wentworth, C., R. Jachens, R. Simpson and A. Michael (1992), Structure of the Parkfield region, CA, from geology and geophysics compiled in a geographic information system. *Eos Trans. AGU, 73*, Fall Meeting Supplement, 396.

Wentworth, C.M. and M.D. Zoback (1989), The style of late Cenozoic deformation at the eastern front of the California coast ranges, *Tectonics, 8*, 237-246.

Wilcox, R., T.. Harding and D. Seely (1973), Basic wrench tectonics, *AAPG Bulletin*, *57* (1), 74-96.

Williams, C. F. and T. N. Narisimhan (1989), Hydrogeologic constraints on heat flow along the San Andreas Fault: A testing of hypotheses, *Earth and Planetary Science Letters, 92*, 131– 143.

Wilson, J., J. Chester and F. Chester (2003), Microfracture fabric of the Punchbowl Fault zone, San Andreas system, California, *Journal of Structural Geology, 25*, 1856-1873.

Wong, T.-f (1990), Mechanical compaction and the brittle—ductile transition in porous sandstones in *Geological Society, London, Special Publications 54*, 111-122.

Wong, T.-f., P. Baud and E. Klein (2001), Localized failure modes in compactant porous rock, *Geophysical Research Letters, 28* (13), 2521–2524.

Wong, T.-f., C. David and W. Zhu (1997), The transition from brittle faulting to cataclastic flow in porous sandstones: Mechanical deformation, *Journal of Geophysical Research, 102* (2), 3009–3025.

Woodburne, M. O. (1975), Cenozoic stratigraphy of the Transverse Ranges and adjacent areas, southern California, *GSA Special Paper 162,* 91 pp.

Zoback, M.D. and J.H. Healy (1991), In situ stress measurements to 3.5 km depth in the Cajon Pass scientific research borehole: Implications for the mechanics of crustal faulting, *Journal of Geophysical Research, 97*, 55039-55058.

Zoback, M.D., M.L. Zoback, V.S. Mount, J. Suppe, J.P. Eaton, J.H. Healy, D. Oppenheimer, P. Reasenberg, L. Jones, C.B. Raleigh, I.G. Wong, O. Scotti, and C. Wentworth (1987), New evidence on the state of stress of the San Andreas Fault system, *Science, 238*, 1105-1111.

Zoback, M., L. Silver, T. Henyey and W. Thatcher (1988), The Cajon Pass scientific drilling experiment: Overview of phase I, *Geophysical Research Letters, 15* (9), 933-936.

APPENDIX 1

FIGURES

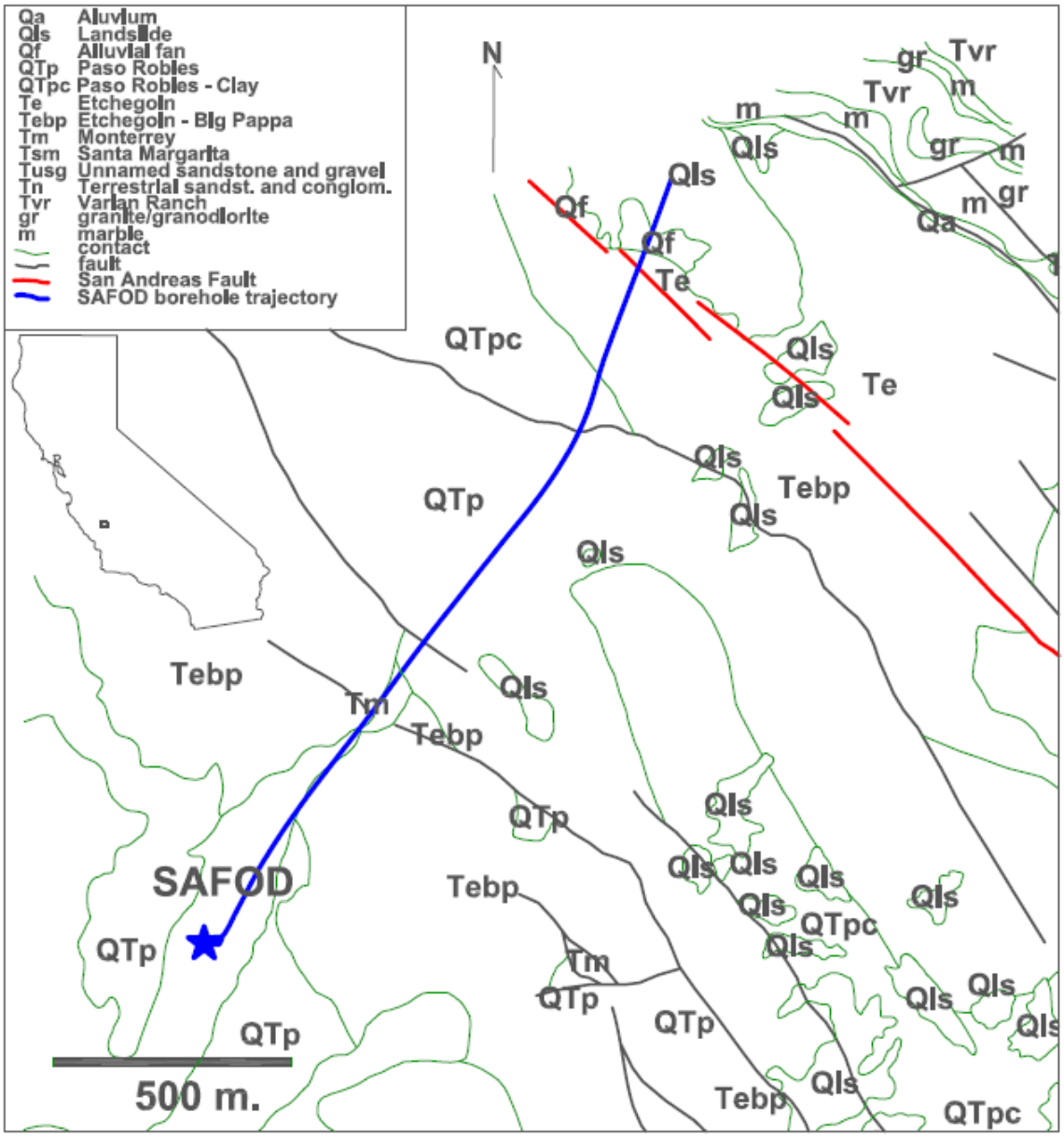

Figure 1. Geologic map of the SAFOD area. Borehole trajectory is shown in blue. Inset shows location in the state of California. Modified from *Thayer et al., 2004*.

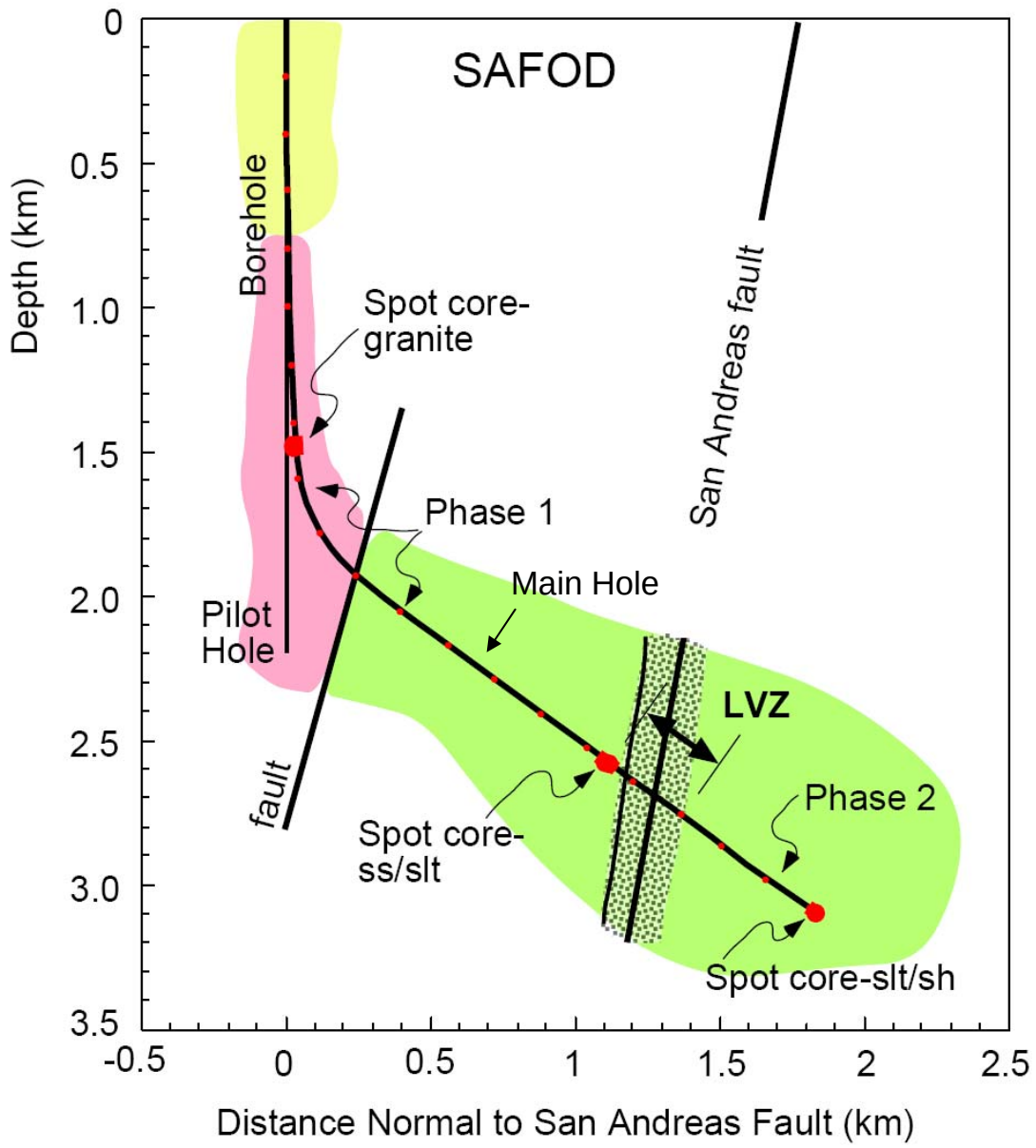

Figure 2. Cross section showing the pilot hole and main borehole at SAFOD. Different lithologies are shown schematically : yellow and green represent sedimentary rocks (ss for sandstone, slt for siltstone, sh for shale); pink represents Salinian granite. Fault locations are approximated with heavy black lines. Phase 1 portion of the main hole borehole terminates at the base of the ss/slt spot core. Phase 2drilling cut across the SAF and terminated at the slt/sh spot core.

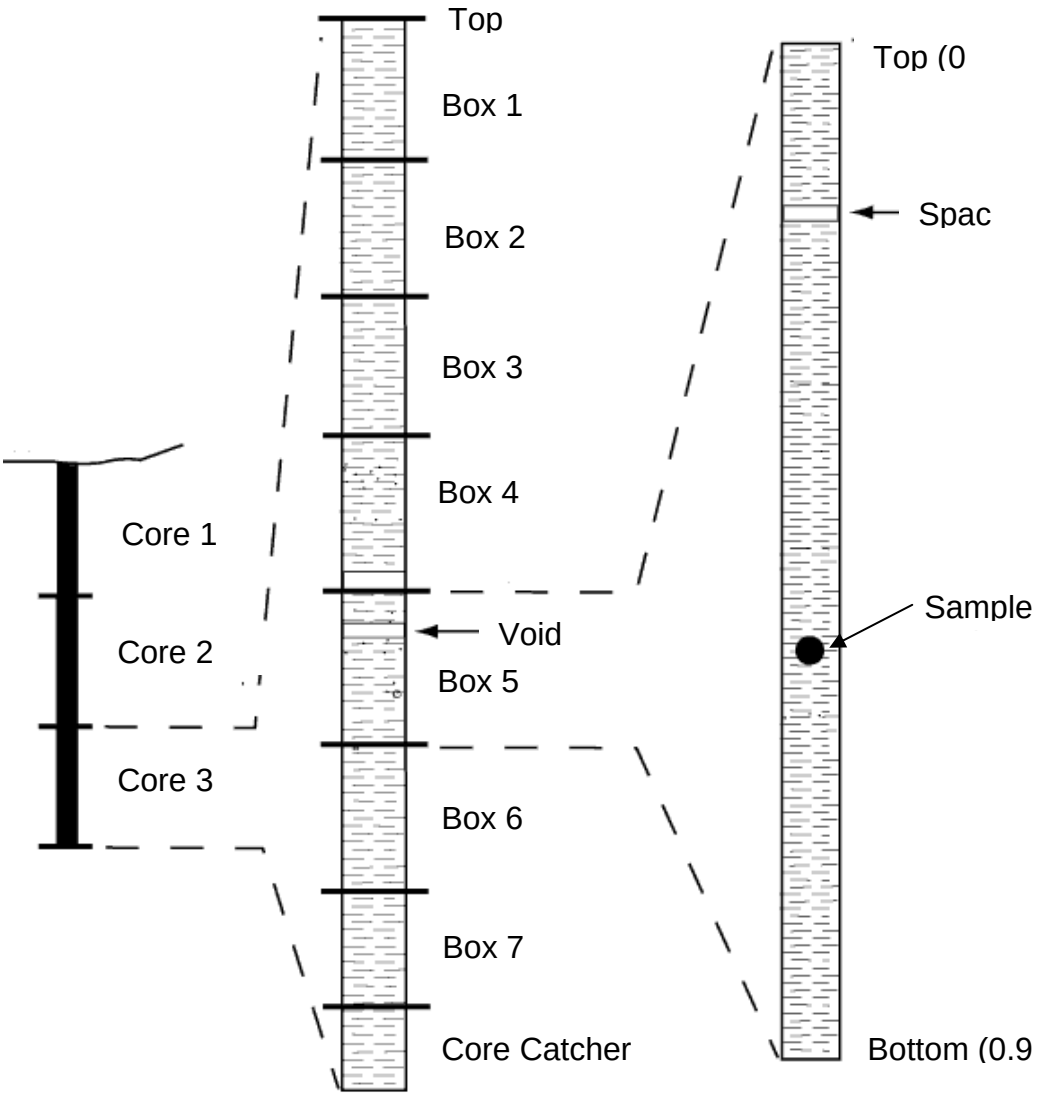

Figure 3. Illustration of the subdivision of spot cores into boxes. The total core is pushed together and subdivided into boxes, 0.9 m long. Spacers are inserted to fill voids between pieces of core. Modified from *Shipboard Scientific Party* [2001]. See also http://www.icdp-online.org/contenido/icdp/front_content.php?idart=1037

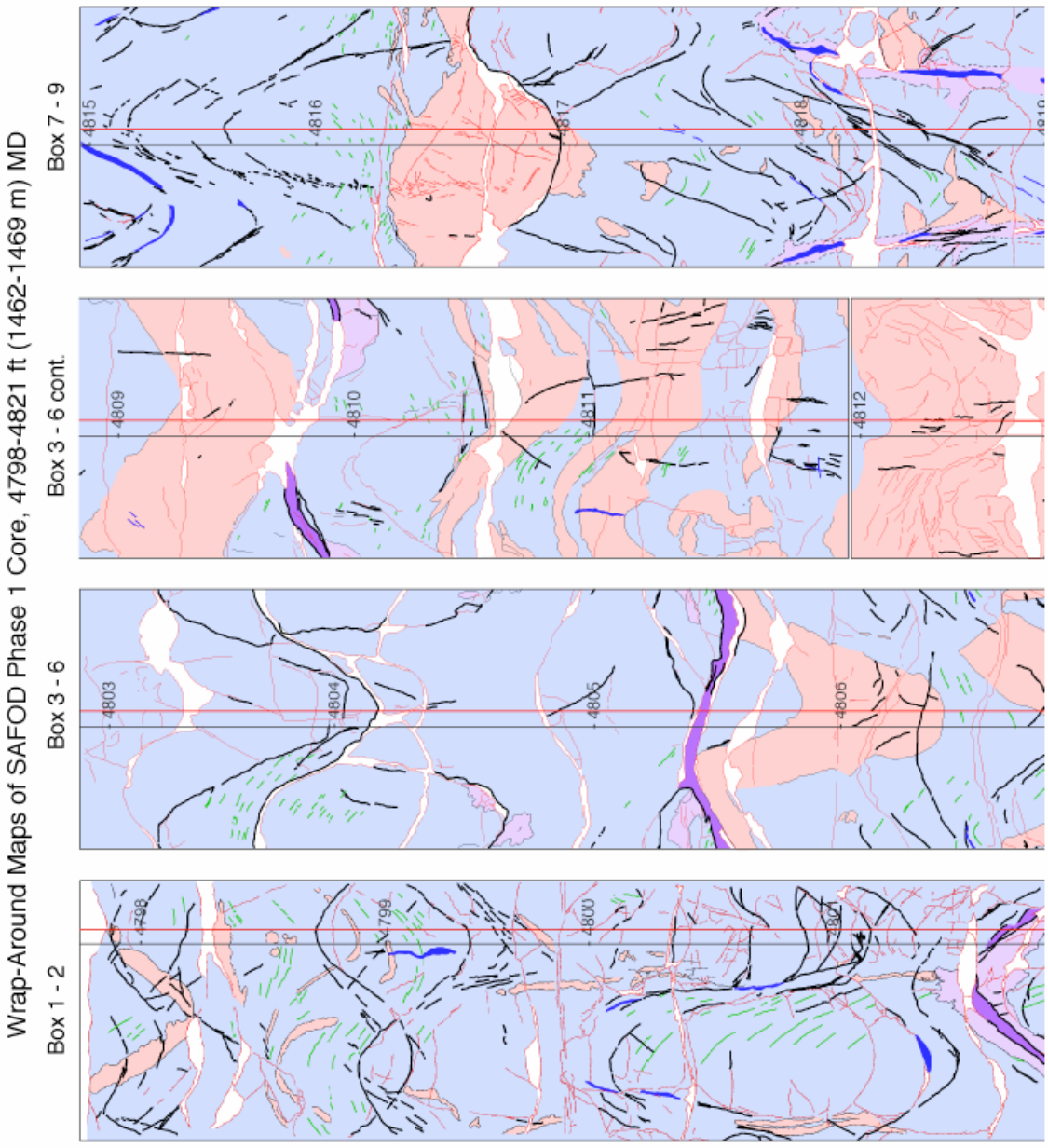

Figure 4. 1:1 wrap-around maps of the granodiorite spot core. Spot core taken from vertical portion of the main borehole during Phase 1 drilling. Three contiguous sections (boxes 1-2, 3-6, 7-9) could be established initially after cleaning and piecing the core back together. Different lithologic and structural features are shown.

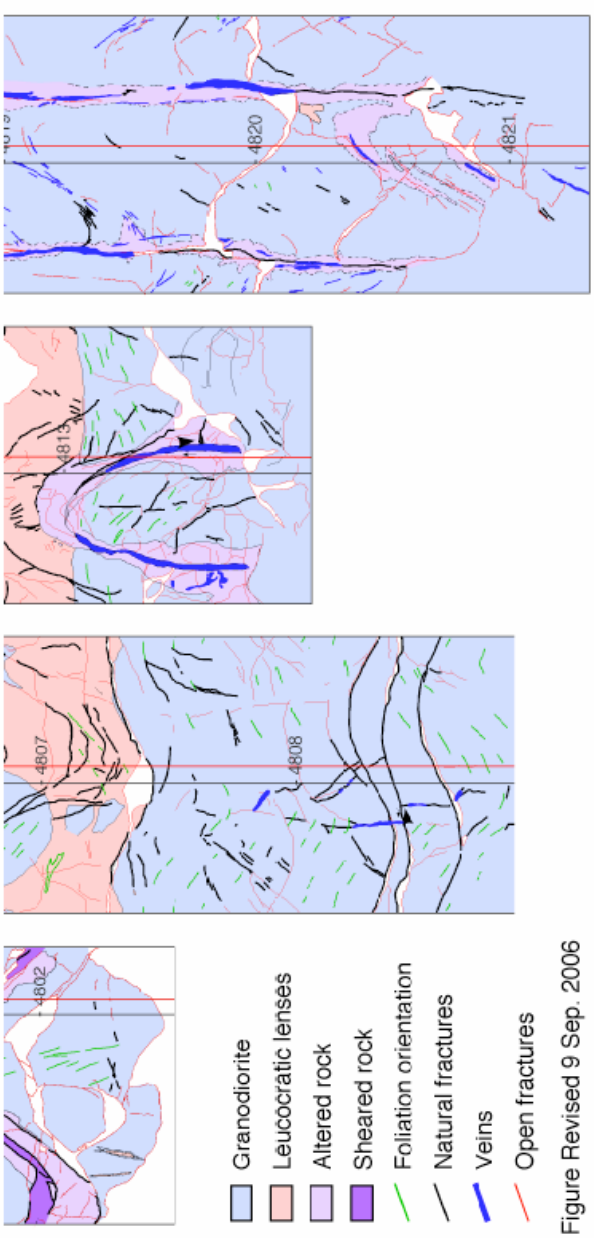

Figure 4. Continued.

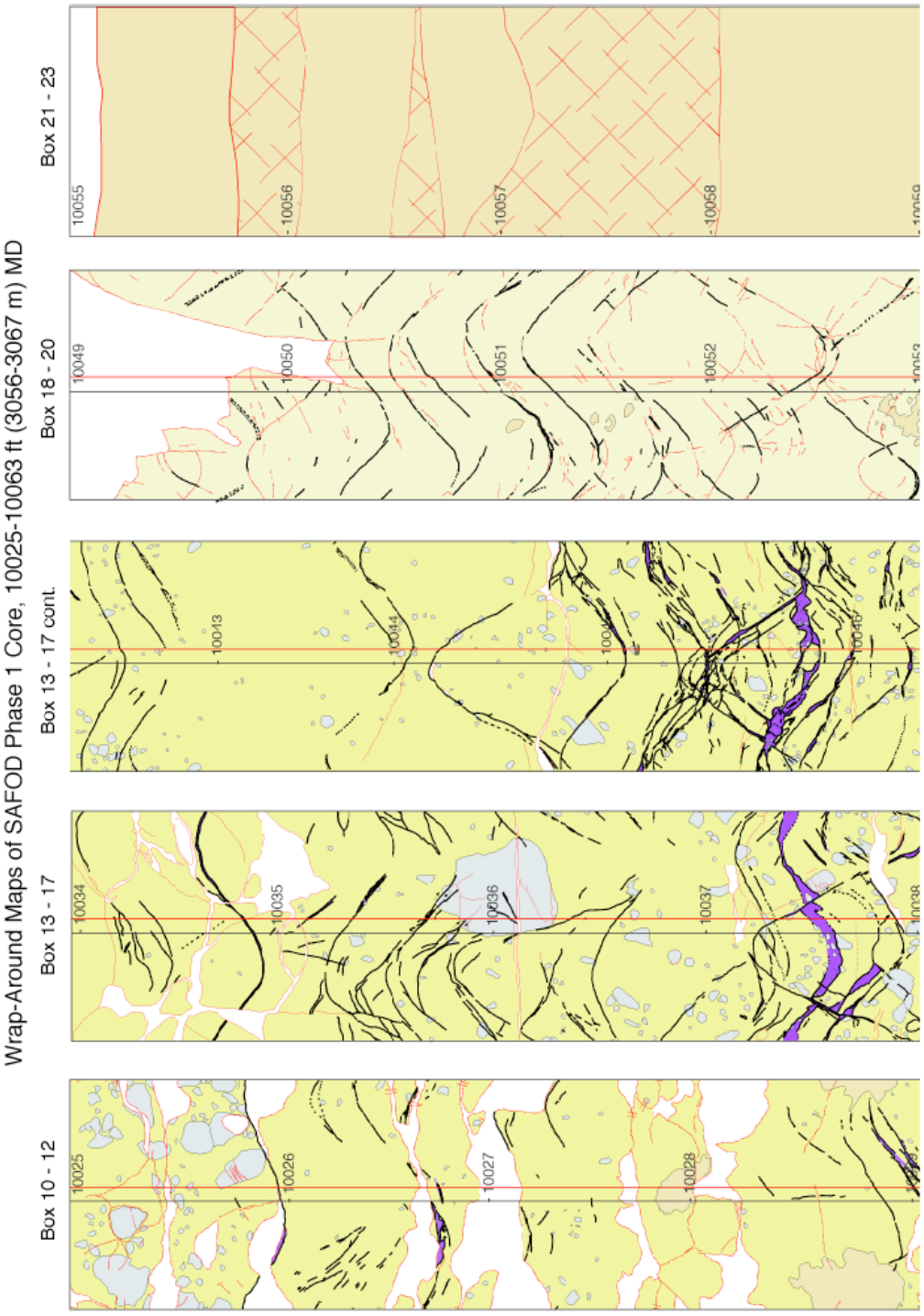

Figure 5. 1:1 wrap around maps of the sedimentary spot core. Lower spot core taken from the deviated portion of main borehole during Phase 1 drilling. Three contiguous sections (boxes 10-12, 13-17 and 18-20) could be established initially after cleaning and piecing the core back together. Different lithologic and structural features are shown.

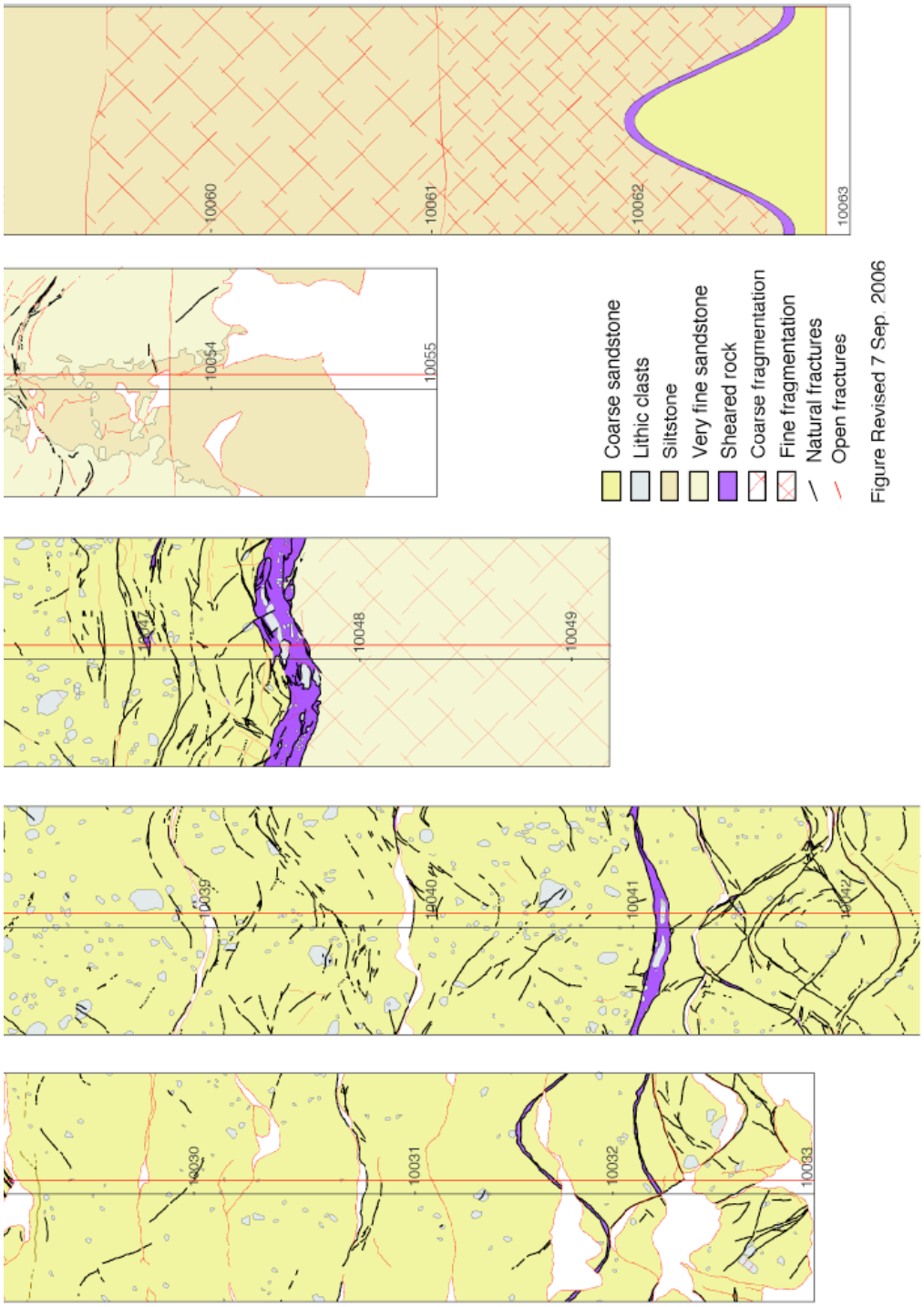

Figure 5. Continued

a.

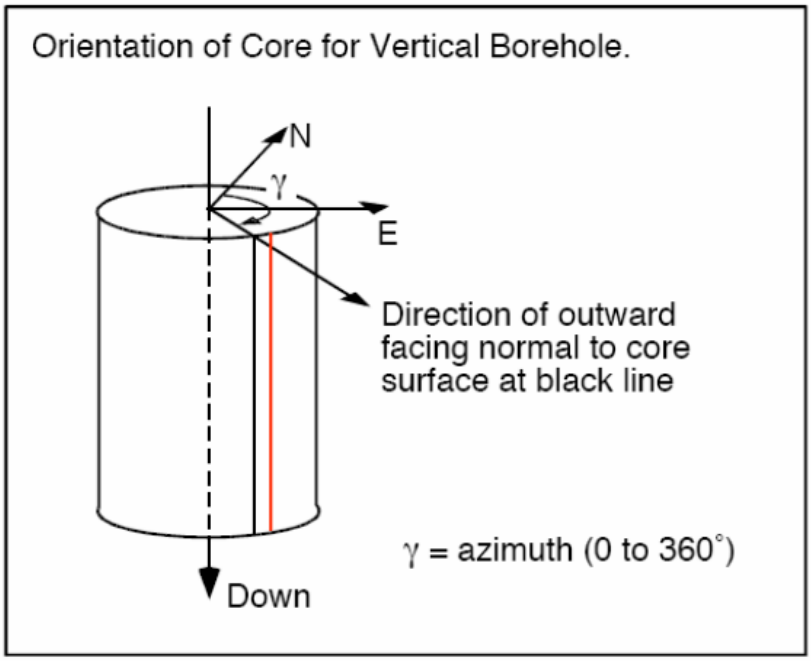

b.

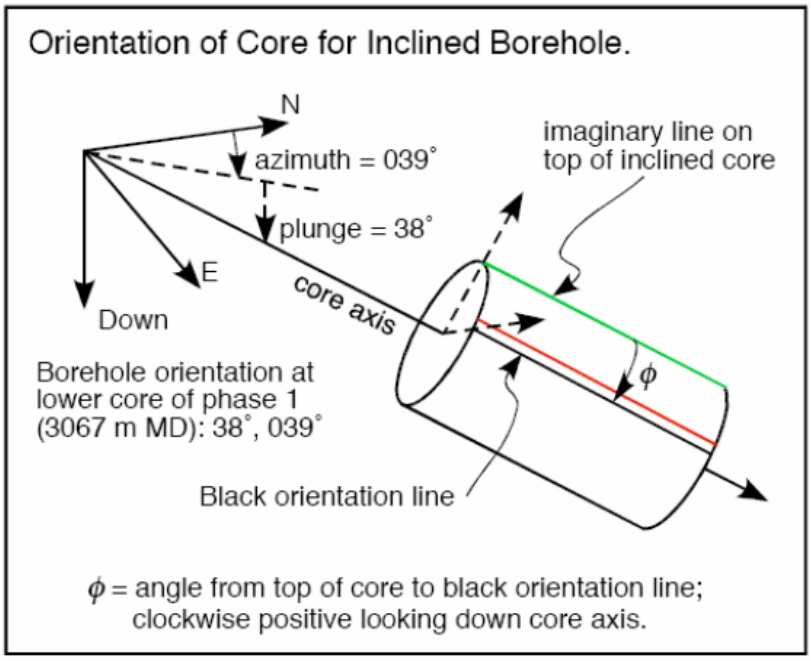

Figure 6.Orientation convention for spot core. a) Upper spot core taken from the vertical portion of the main borehole during Phase 1 of drilling. b) Lower spot core taken from the inclined portion of the main borehole during Phase 1 drilling. Core axis inclination is 039°, 38°. Orientation of the spot core in geographic and reference frame requires knowing the orientation of the

borehole and the angles γ and Φ .

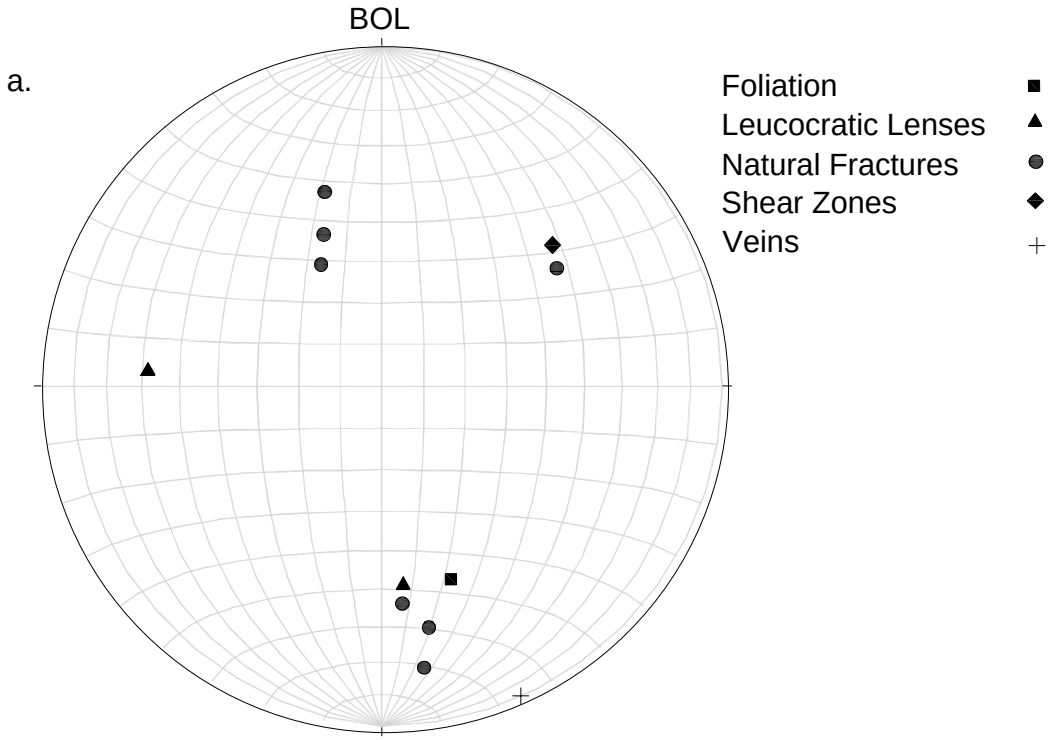

Figure 7. Mesofabric deformation features and lithologic layering from granodiorite spot core in each contiguous section. Lower-hemisphere equal-area projections with black orientation line (BOL; see Figure 4) at top. Number of data indicated. a) Boxes 1-2. b) Boxes 3-6. c) Boxes 7-9.

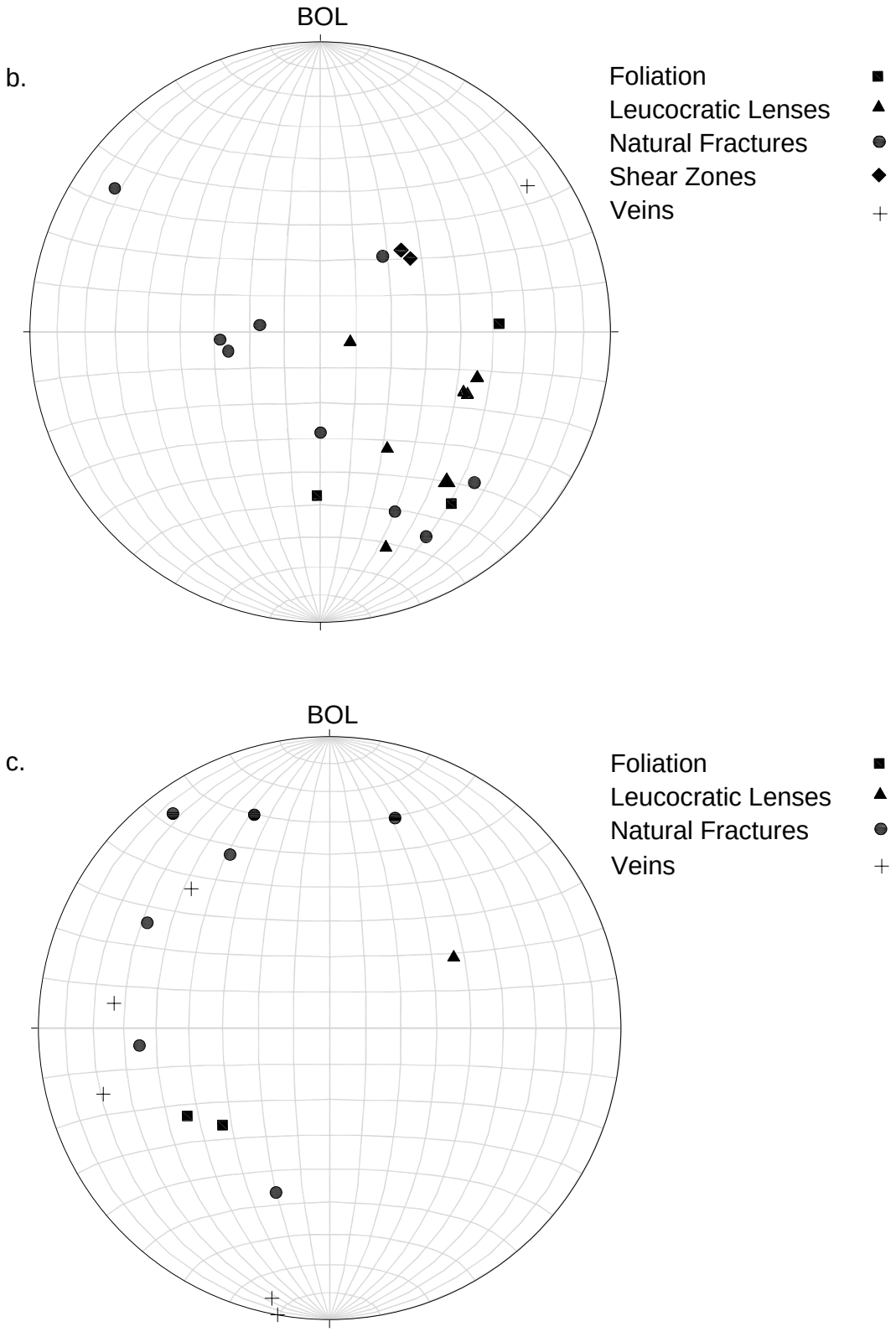

Figure 7. Continued.

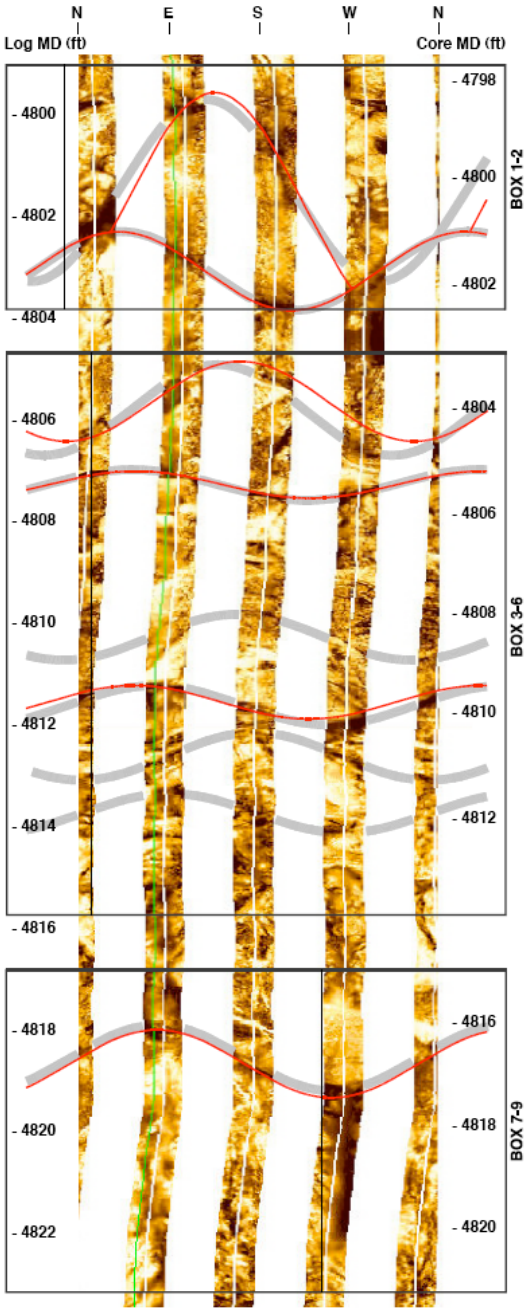

Figure 8. FMI logs of the main borehole wall over the depth interval corresponding to the upper spot core from Phase 1. Thick gray lines highlight the major planar features evident in the FMI logs that can be correlated with mesoscale fractures on the outer surface of the spot core (represented by thin red sinusoids). Measured depths for the FMI logs are shown on the left. Measured depths for spot core are shown on the right. The depth range of each contiguous section of the spot core is indicated by the rectangles, and the vertical line marks the position of the black orientation line drawn down the axis of the spot core (see Figure 5).

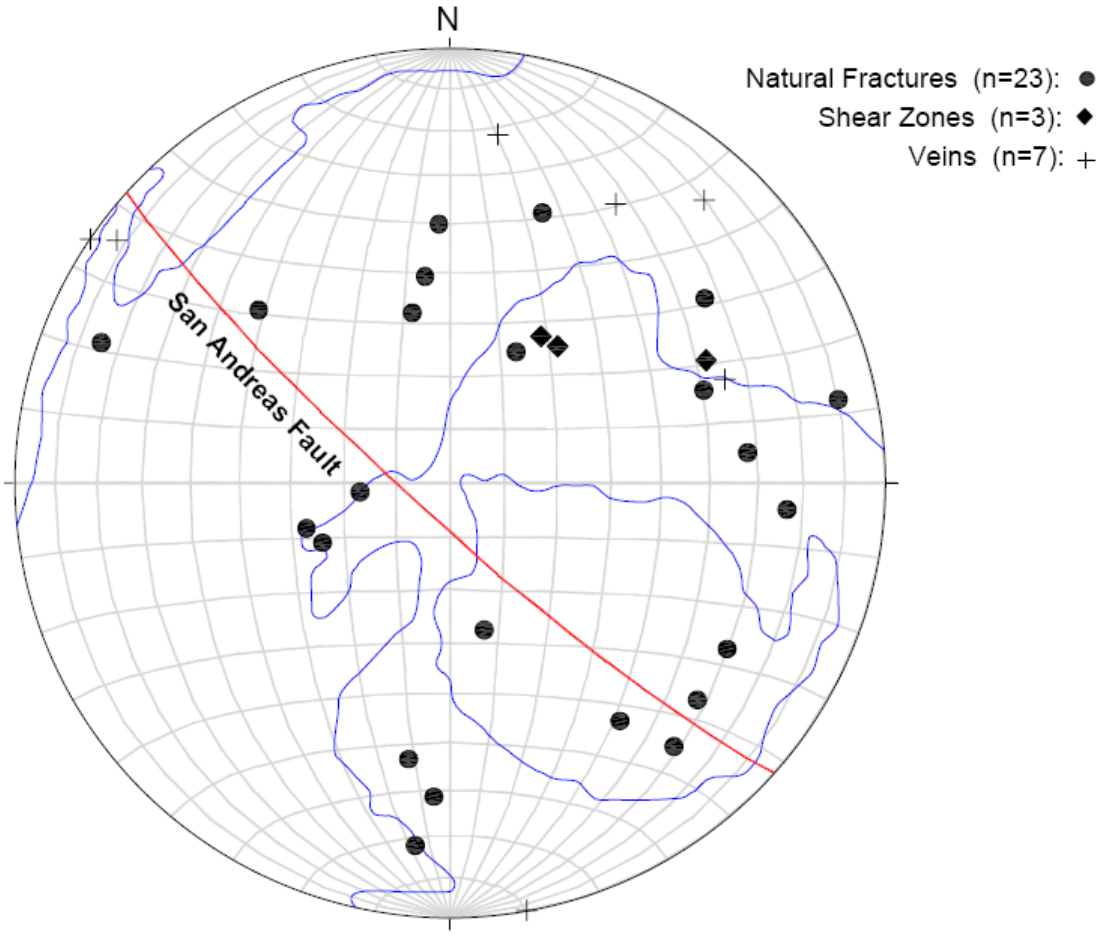

Figure 9. Poles to mesoscale fractures and lithologic layering from the granodiorite spot core. Metamorphic and igneous layering is contoured using Kamb method with two sigma contour interval. Poles to natural fractures, shear fractures, veins and the SAF orientation are plotted individually in a lower-hemisphere, equal-area projection with North (N) at top.

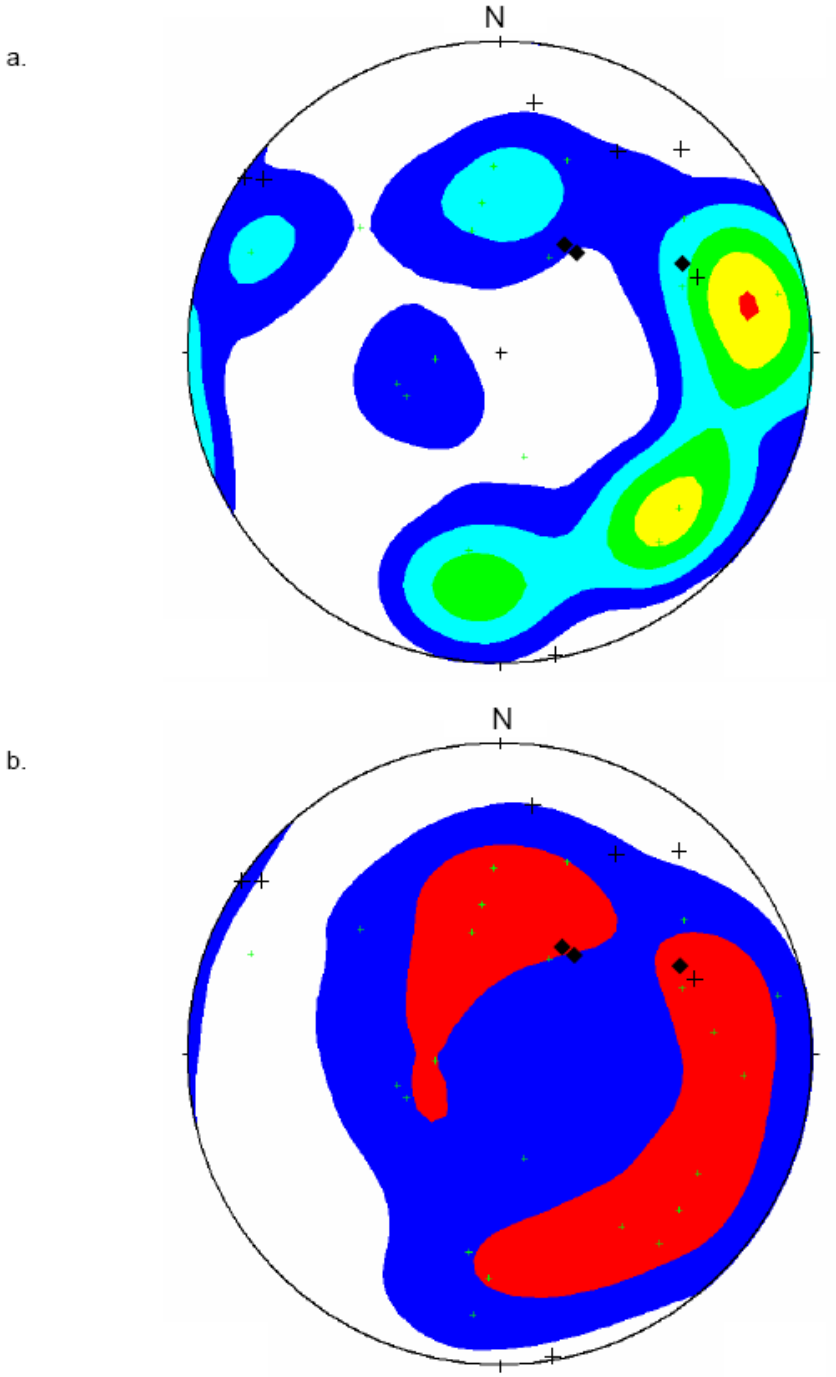

Figure 10. All mesoscale fractures in upper spot core of Phase 1. Poles to veins (crosses) and shear zones (solid diamonds) plotted in a lower-hemisphere equal-area projection with North (N) at the top. Overlying these data are contours of the poles to all natural fractures using the Kamb contouring method with a two sigma contour interval. a) Natural fractures are weighted (see page XX). b) Natural fractures are unweighted.

a.

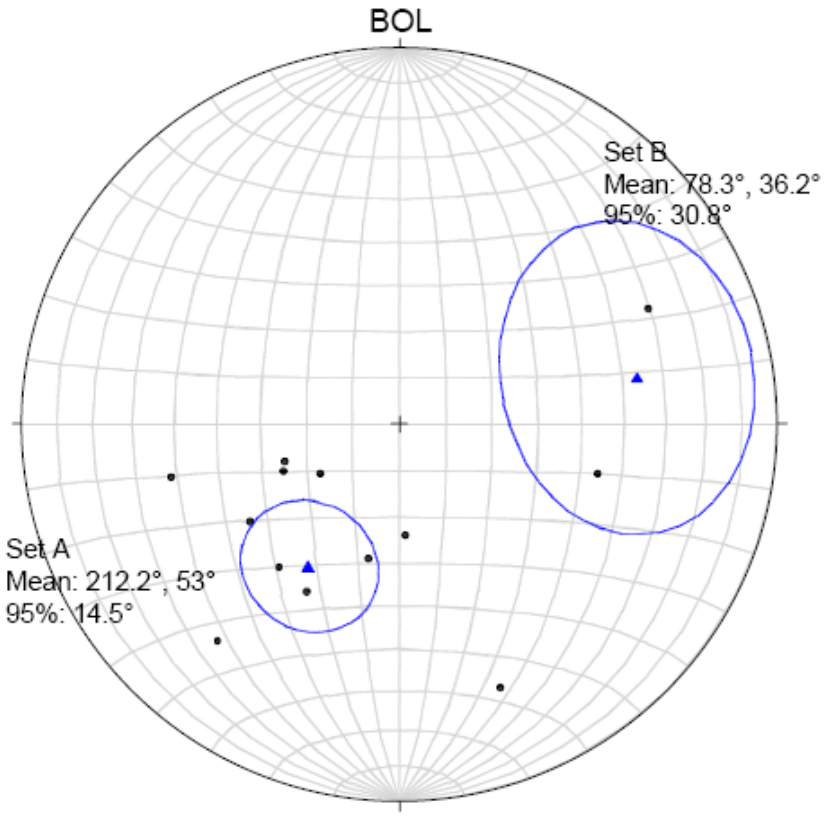

Figure 11. Poles to mesoscale fractures (solid circles) cutting the lower sedimentary spot core. Data are plotted in lower-hemisphere equal-area projections with black orientation line (BOL, see Figure 4) at top. Mean vector (solid triangle) and 95% confidence cone (in blue) is plotted for each set. a) Boxes 10-12, b) Boxes 13-17, c) Boxes 18-20.

b.

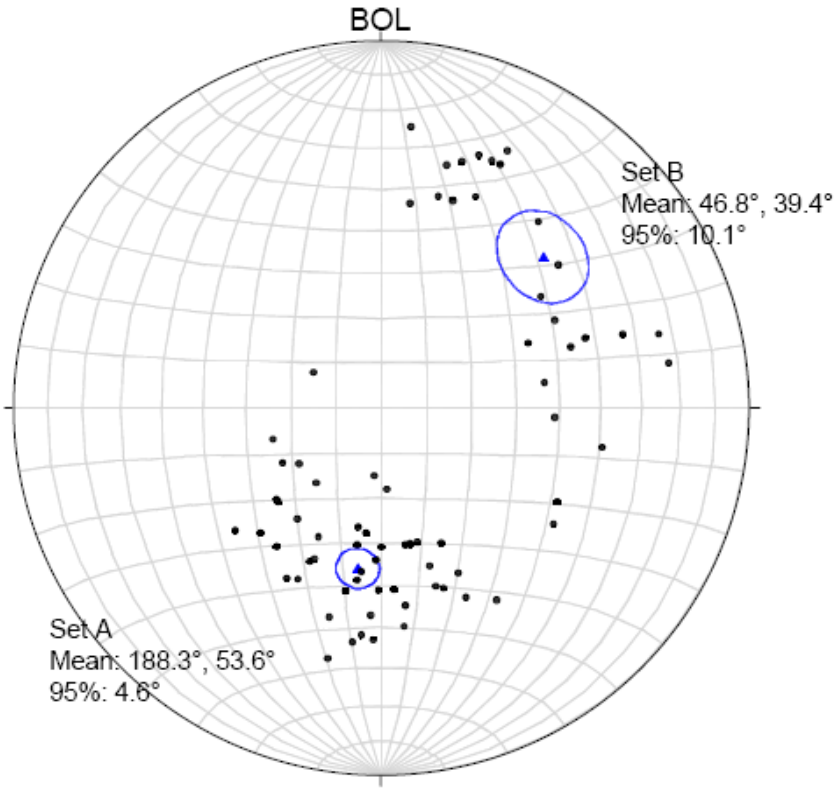

c.

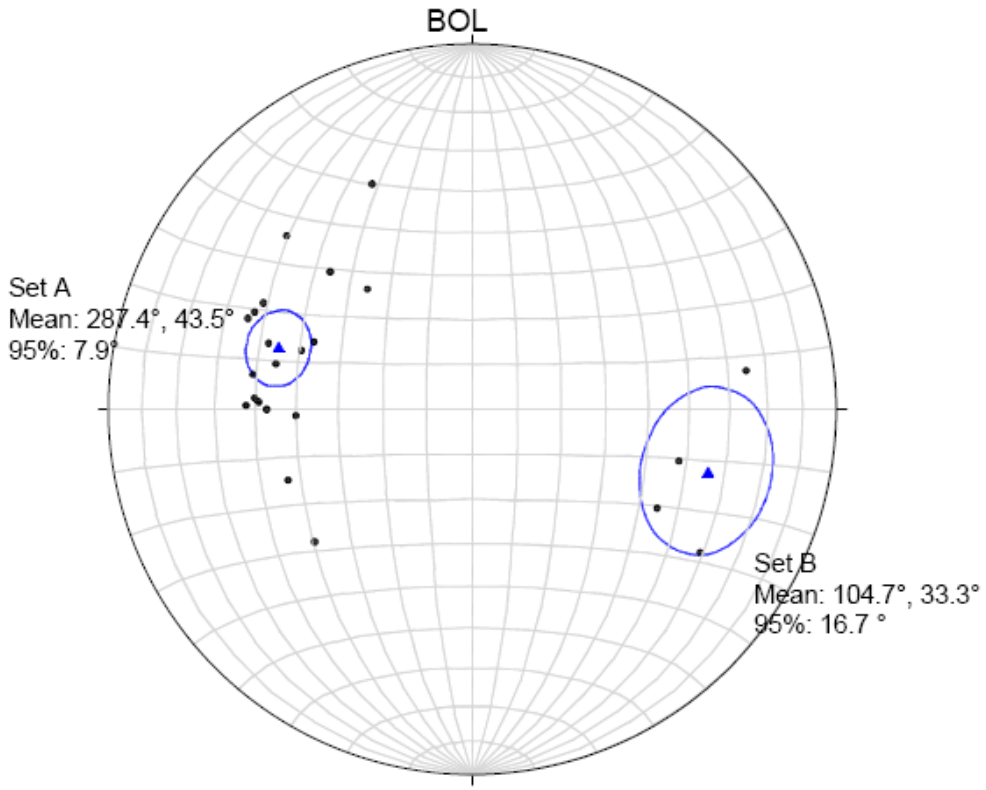

Figure 11. Continued.

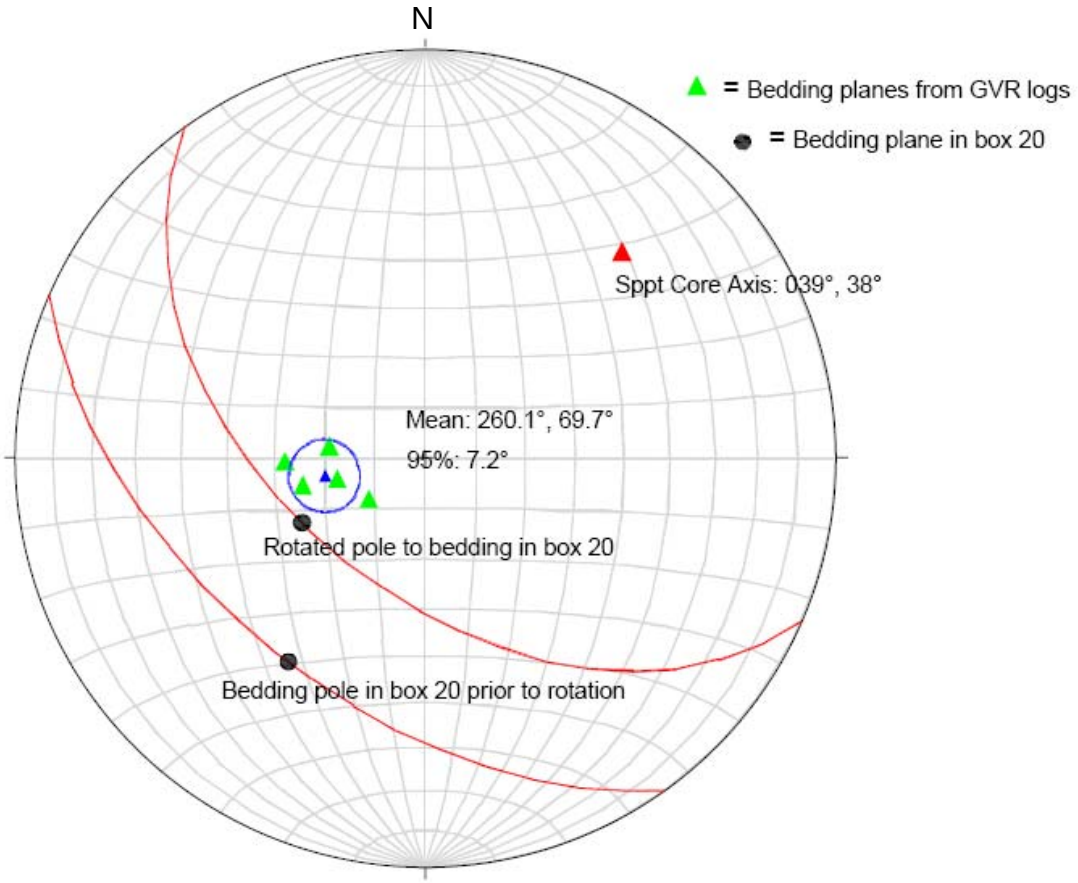

Figure 12. Poles to bedding planes observed in LWD-GVR image logs and to the bedding plane measured in box 20 (Figure 5). All possible orientations of the bedding plane in box 20 are represented by the red small circle. Mean vector (solid blue triangle) of poles to bedding observed in LWD-GVR logs (sloid green triangles) is also plotted. Lowerhemisphere, equal-area projection with north (N) at top.

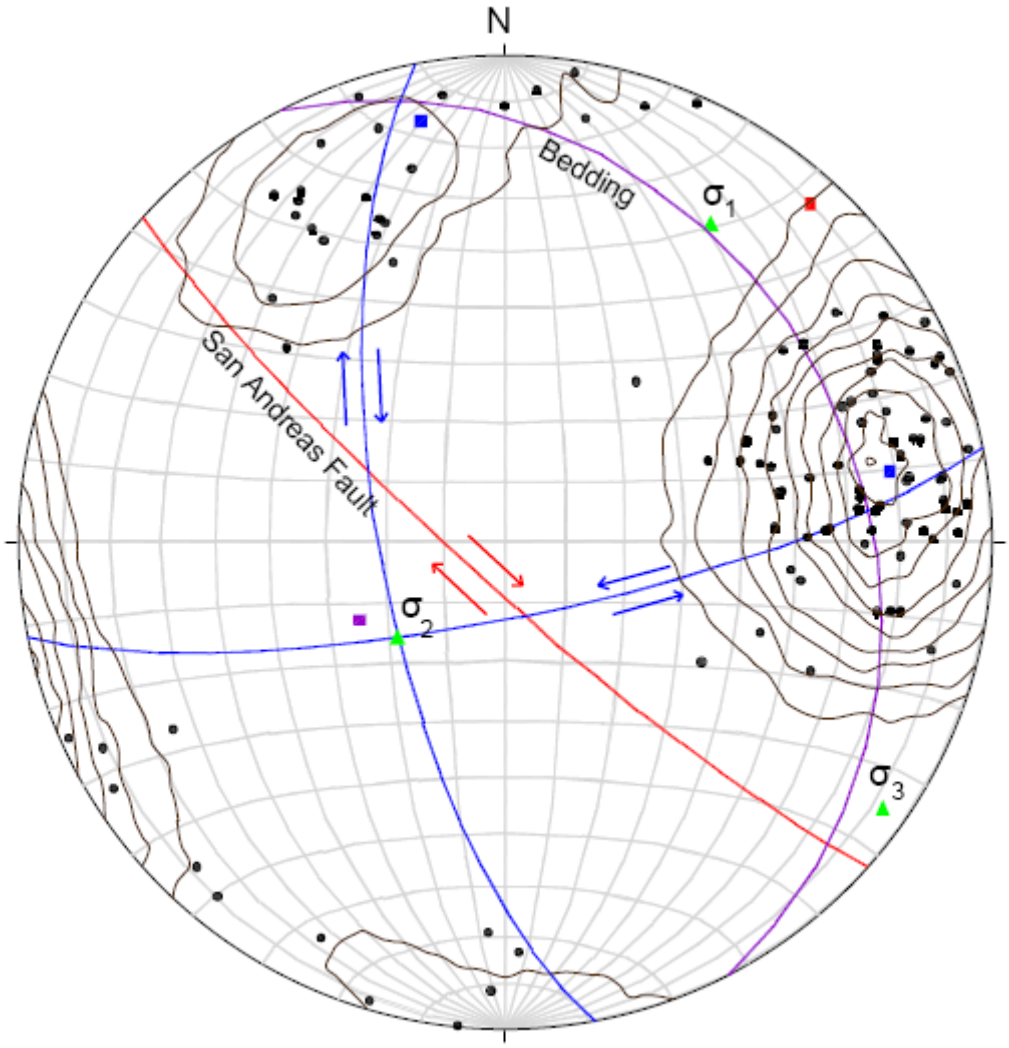

Figure 13. Summary diagram of all mesoscale fractures measured in the lower sedimentary spot core. Poles to fractures (solid circles) are plotted in a lowerhemisphere equal-area projection with North (N) at top. Pole data are also contoured using Kamb method with a two sigma contour interval. The best fit planes to each concentration are shown by the blue great circles. The SAF planeis shown by the red great circle and the pole to the plane, by the red square. The principal compressive stresses (green solid triangles) are oriented: σ_1 = 23.3°, 032.8°, σ_2 = 65.9°, 228.4° and σ_3 = 05.7°, 125.3°.

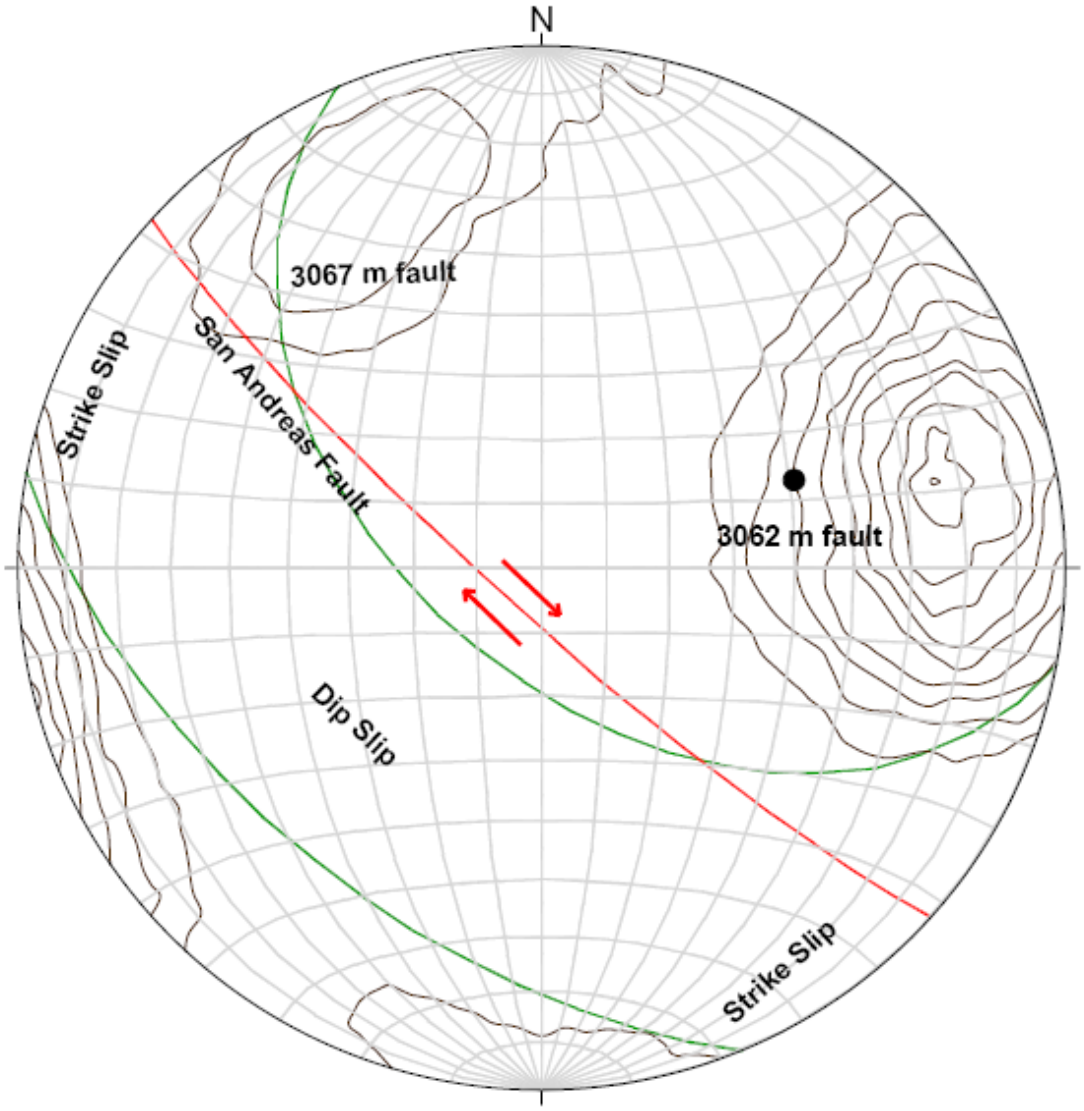

Figure 14. Orientations of two largest subsidiary faults cutting lower spot core. Poles to fractures are contoured using Kamb method with a two sigma contour interval. The SAF is shown by a red great circle. The pole of fault at 3062 m MD is given by the solid black circle and a green small circle representing all possible orientations of 3067 m MD fault pole are also shown. The zones of dip-slip and strike-slip kinematics for the 3067 m MD fault are indicated. Plot is a lower hemisphere, equal-area projection with North (N) at top.

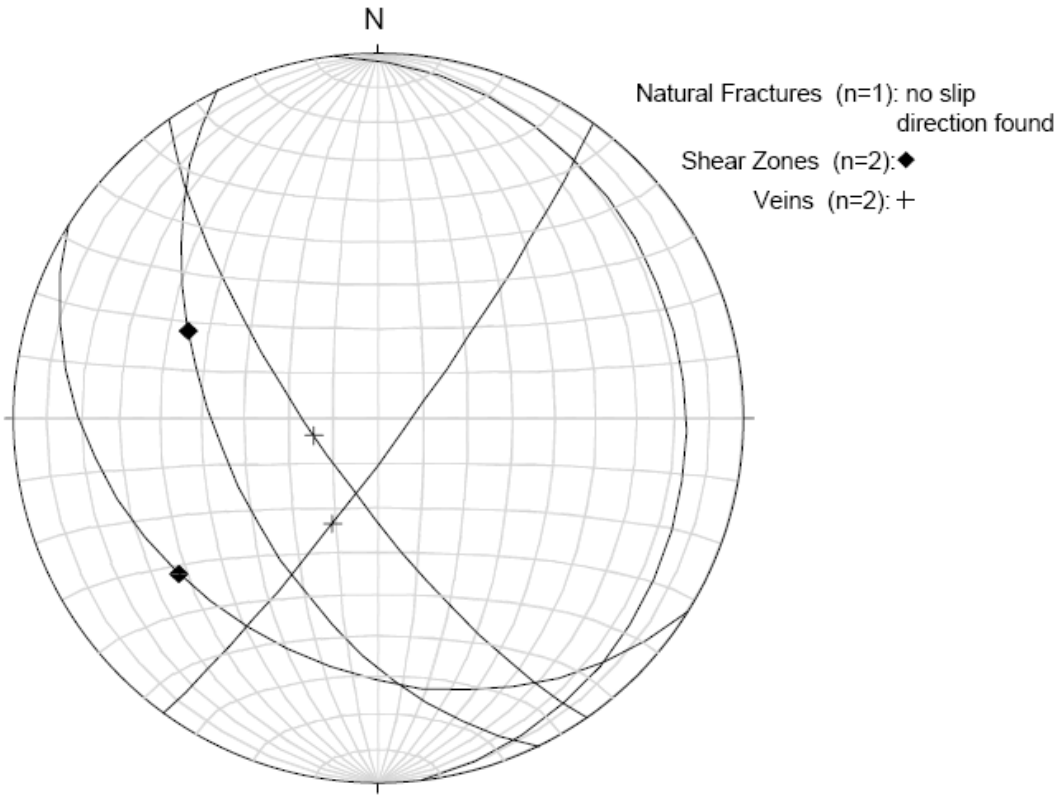

Figure 15. Planes with measured slip vectors in the sedimentary spot cores. Planes are represented by great circles plotted in a lower-hemisphere, equal-area projection with North (N) at top. These slip vectors were measured on shear zones and veins. The measured slip vector is plotted on each great circle (a diamond for the shear zones and a cross for the veins). No measurable slip vector was found in the natural fracture, however, normal separation was evident (see Table 8).

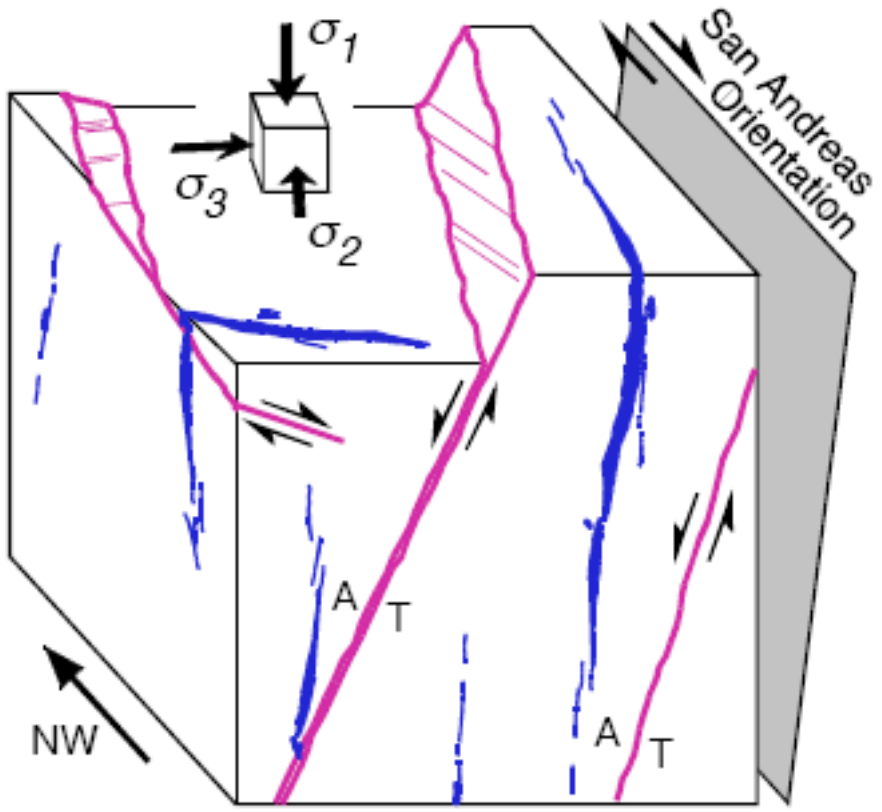

Figure 16. Schematic block diagram of the structural features in the granodiorite spot core. Subvertical veins are shown in blue. The low angle shear zones and shear fractures are shown in pink. The SAF orientation, kinematics and inferred paleostress state are shown.

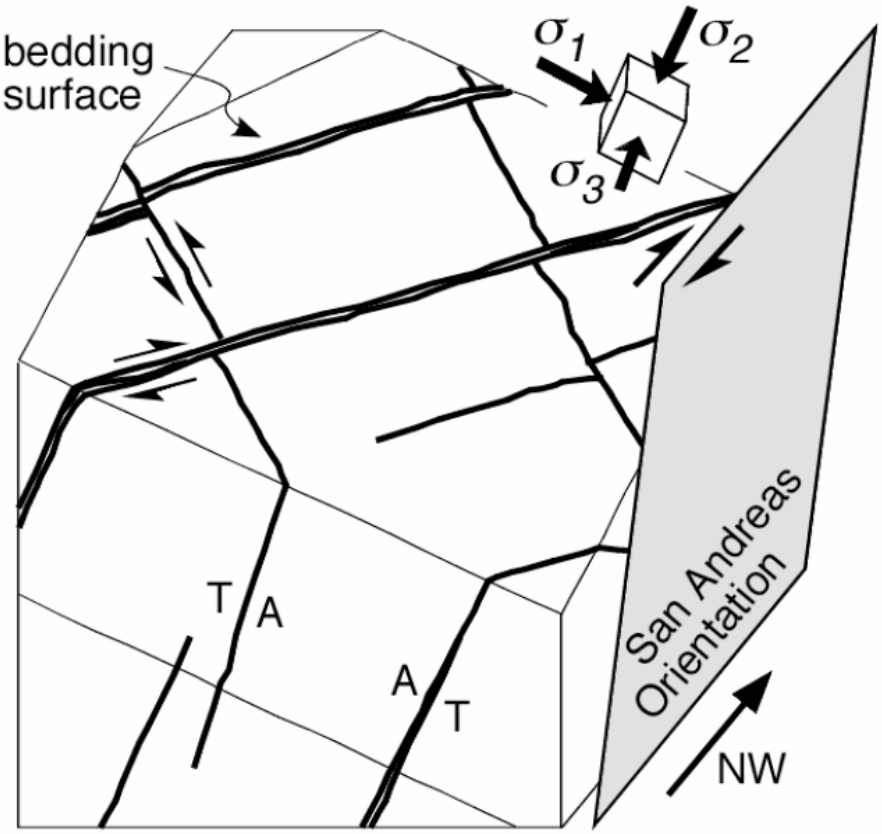

Figure 17. Schematic block diagram of structural features in the sedimentary spot core. Bedding orientation, conjugate faults (T is towards, A is away), SAF orientation, kinematics, and inferred paleostress state are shown.

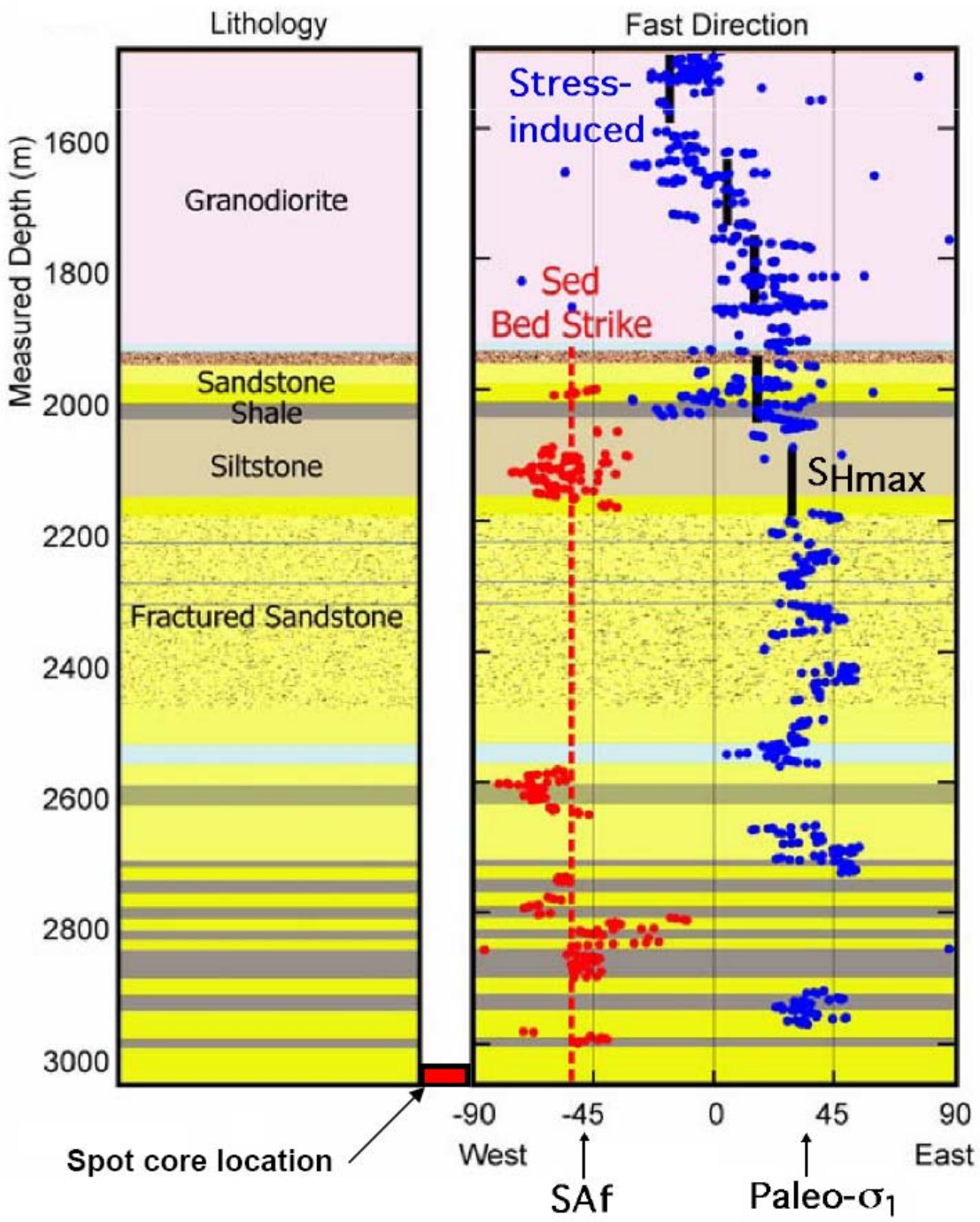

Figure 18. In-situ stress measurements compared to inferred maximum principal compressive paleostress direction from lower sedimentary core. The maximum principal compressive stress direction in SAFOD borehole is estimated using fast shear wave direction. The spot core is shown at ~ 3000 m MD. The azimuth of the SAF, and the paleo- σ_1 azimuth inferred from the lower sedimentary spot core are indicated by arrows at the base of the figure and are approximately orthogonal. Modified from *Boness and Zoback, 2006*.

APPENDIX 2

TABLES

Table 1. Some general geologic observations from the SAFOD Main borehole [a]

Measured Depth	General Observation
Surface - 768 m	Tertiary sedimentary rocks. All depths are measured depths relative to the rig floor (sometimes referred as KB) located 31' above ground.
768 m -1923 m	Drilled through fractured granitic rock. A core was obtained from 4798'-4824' consisting of granodiorite with numerous fractures and faults.
1923 m	Drilled out of granitic rock into sedimentary rock. Apparently mostly arkosic sandstone and conglomerates
1923 m -3158 m	Alternating units of arkosic rocks with fine-grained, bedded sediments. From 10,025' to 10,063' a core was obtained at the end of Phase 1. The core consisted mostly of arkosic sandstone/conglomerate granitic clasts with a clay rich fault near the bottom at 10062'.
3158 m	Marked change in lithology. Shale and siltstones encountered that will constitute the dominant lithologies to the bottom of the hole.
3322 m	First serpentine found in cuttings. Below 10,940' serpentine only found occasionally.
3341 m	Big gas kick and short drilling break – fault zone?
3414 m - 3490 m	Apparently folded sediments seen in GVR image collected by LWD tool
3493 m - 3642 m	Long (~500') coherent interval of steeply dipping bedding. Dip is 60-80º to the NNE. While ~500' is an apparent thickness, the trajectory of the hole (~N20Eº, 54º from vertical) is at a high angle to the bedding
3703 m	Gas starts increasing, esp. H2, Radon and CO2
Below 3800 m	Several fragments of Inoceramus, a Mesozoic fossil are found by mud loggers in the cuttings
3990 m - 3997.5 m	12' of core recovered (of 25' drilled) from bottom of hole. Interbedded shales, siltstones and very fine sandstones. Large fragment of Inoceramus in the core. Some evidence of bioturbation found .

[a] Zoback, written comm., 2006

Table 2. Orientation of black line on granodiorite spot core 1462-1470 m MD

Box Numbers	Azimuth[1]
1-2	346˚
3-6	013˚
7-9	246˚

[1]Relative to North looking down core axis with clockwise positive (right hand rule) as shown in Figure 6.

Table 3. Orientation and weighting factor of fractures[a] in the granodiorite spot core.

Feature	Orientation (strike, dip)	Weight
V	259.9˚, 90.0˚	10.00
V	131.9˚, 76.3˚	4.22
V	120.6˚, 63.6˚	2.25
V	097.8˚, 69.8˚	2.90
V	159.2˚, 56.9˚	1.83
V	036.1˚, 84.2˚	9.95
V	034.1˚, 90.0˚	10.00
S	154.3˚, 54.8˚	1.74
S	121.7˚, 32.5˚	1.19
S	127.8˚, 32.9˚	1.19
N	083.0˚, 39.6˚	1.30
N	077.4˚, 33.0˚	1.19
N	087.5˚, 49.9˚	1.55
N	278.6˚, 54.0˚	1.70
N	273.0˚, 61.4˚	2.09
N	275.5˚, 72.6˚	3.34
N	159.9˚, 52.0˚	1.63
N	229.7˚, 68.3˚	2.70
N	234.5˚, 56.7˚	1.82
N	021.9˚, 75.4˚	3.97
N	116.5˚, 27.6˚	1.13
N	211.4˚, 63.4˚	2.23
N	257.0˚, 28.4˚	1.14
N	342.5˚, 28.4˚	1.14
N	353.5˚, 17.1˚	1.05
N	335.0˚, 26.5˚	1.12
N	174.1˚, 58.1˚	1.89
N	184.5˚, 66.6˚	2.52
N	042.1˚, 49.6˚	1.54
N	221.3˚, 64.5˚	2.32
N	108.8˚, 55.3˚	1.76
N	144.0˚, 61.5˚	2.09
N	167.8˚, 80.3˚	5.95

[a] N, natural fractures; S, shear fractures; V, veins

Table 4. Angular relations[1] for alignment of sandstone spot core 3056-3067 m MD

Box Numbers	Angle[2]
10-12	67˚
13-17	86˚
18-20	0˚ (reference)

[1]Determined from weighted best-fit alignment of fracture fabrics.
[2]Relative to black scribe on boxes 18-20 looking down core axis with clockwise positive (right hand rule).

Table 5. Cluster analysis results for the data of the sedimentary spot core.

Set	Rn[e]	κ[f]	Mean Vector	Dihedral Angle
A[a]uw[b]	0.939	16.3	279.9°, 53.2°	98.3°.
B[c] uw	0.89	8.77	132.4°, 41.4°	
Aw[d]	0.935	15.3	279.5°, 51.2°	93.8°.
Bw	0.889	8.73	129.6°, 38.8°	

[a] Set A, 77 data points
[b] uw, unweighted
[c] Set B, 32 data points
[d] w, weighted
[e] Rn, measures preferred orientation
[f] κ, measures dispersion

Table 6. Orientation of bedding in the 3058.5-3061 m MD interval from image logs[1].

Depth[2] (m - MD)	Orientation (dip, dip direction)
3058.5	24.8˚, 077.2˚
3059.1	18.3˚, 075.9˚
3059.4	27.8˚, 088.1˚
3059.7	19.1˚, 095.8˚
3060.1	14.5˚, 053.2

[1]LWD-GVR, Logging While Drilling, GeoVision Resitivity; data from M. Zoback (2005).
[2]Note that depth on GVR logs appear 3 m greater than those for equivalent points on FMI logs for phase 2)

Table 7. Orientation[1] of black line on sandstone spot core 3056-3067 m MD

Box Numbers	Angle[2]
10-12	-118˚
13-17	-137˚
18-20	156˚

[1]Determined from alignment of bedding in Boxes 18-20 to that in borehole determined from image logs.
[2]Relative to top of borehole looking down core axis with clockwise positive (right hand rule) as shown in Figure 11.

Table 8. Kinematic data for granodiorite spot core 1462-1469 m MD

Feature	Box.	Sinusoid number	Plane orientation (strike, dip)	Slip orientation (trend, plunge)	Notes
N	3-6	20	353.5˚, 17.1˚	N/A	Normal separation on fracture
S	1-2	16	154.3˚, 54.8˚	294.7˚, 42.1˚	Right-normal oblique slip
S	3-6	9	121.7˚, 32.5˚	232˚, 31.4˚	-
V	3-6	38	131.9˚, 76.3˚	254.9˚, 75.2˚	Right-normal oblique slip
V	7-9	13	036.1˚, 84.2˚	203.4˚, 64.3˚	-

APPENDIX 3

1:1 MAPS OF GRANODIORITE SPOT CORE

WITH BEST FIT SINUSOIDS

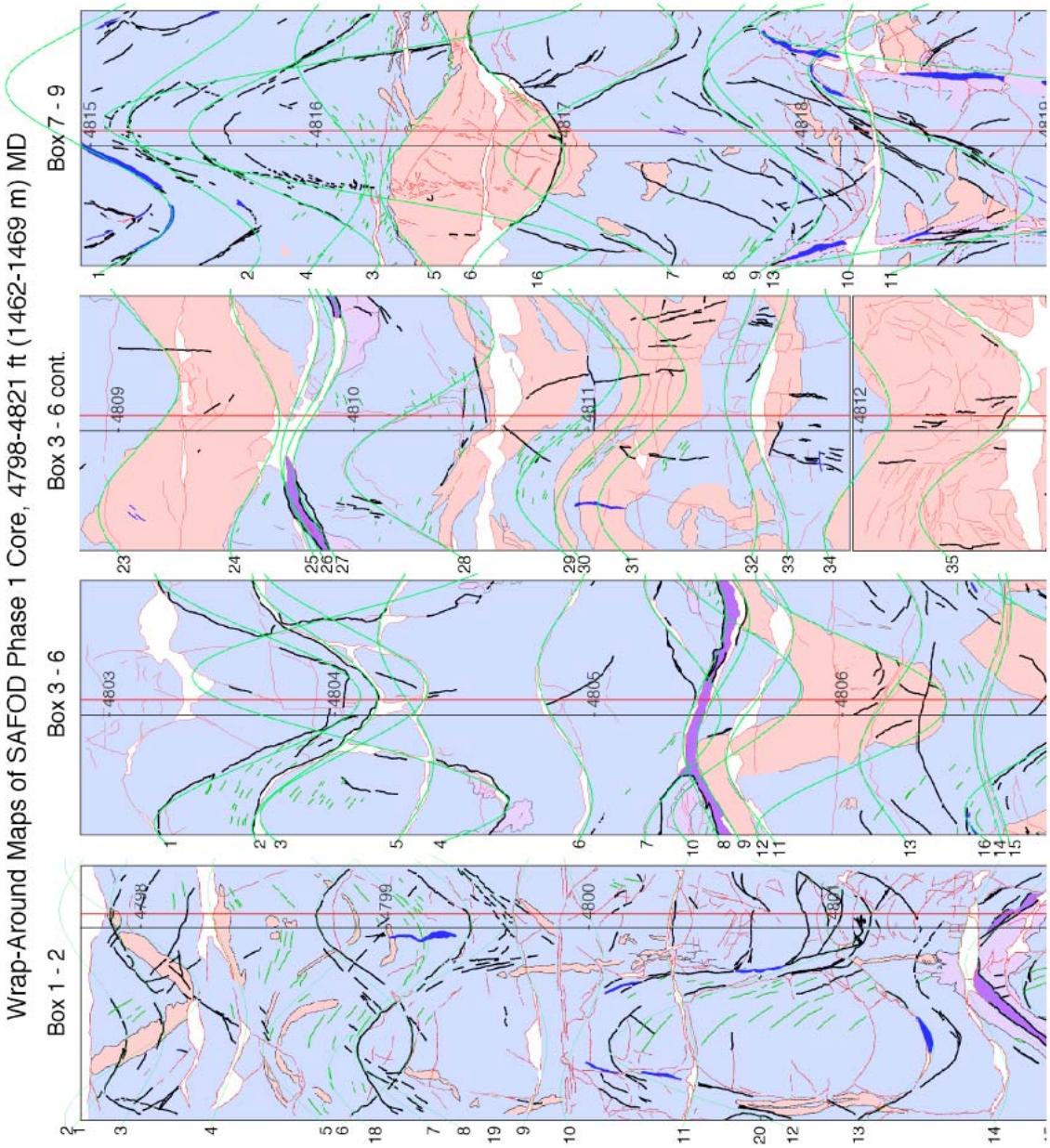

Figure 19. 1:1 maps of granodiorite spot core showing sinusoid fits to each planar feature (Table 9).

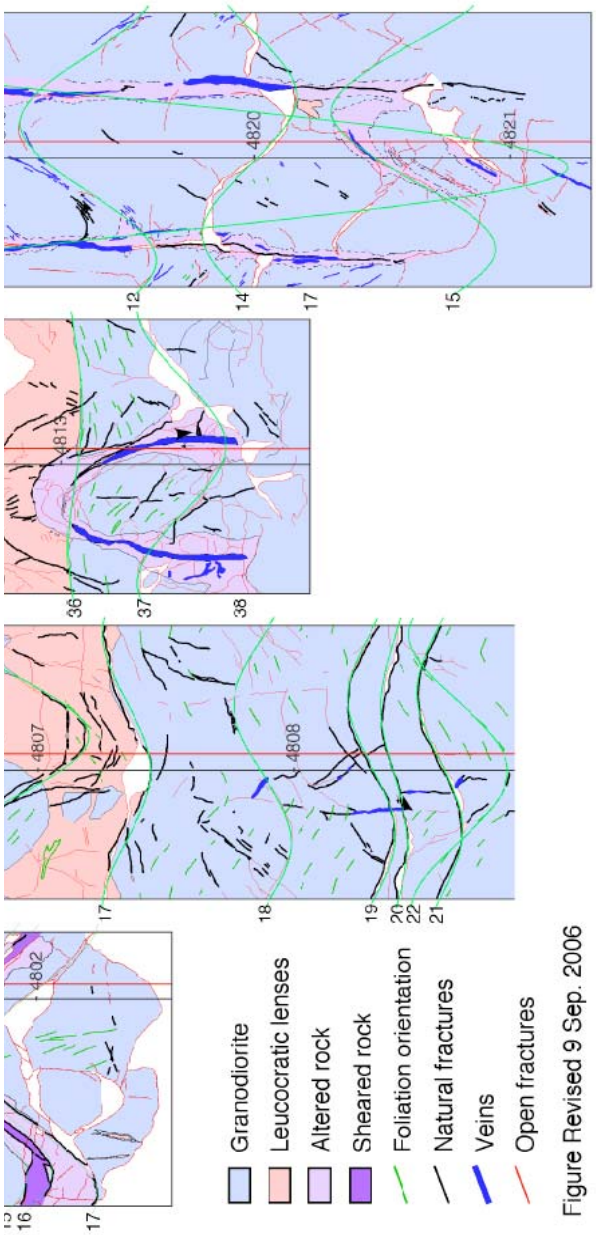

Figure 19. Continued.

Table 9. Orientation of all features noted on granodiorite spot core with respect to geographic North

Box Number	Sinusoid Number	Feature	Strike	Dip
1-2	1	N	83.0	39.6
	2	L	17.9	58.5
	3	N	77.4	33.0
	4	O	56.0	25.2
	5	L	277.8	49.1
	6	N	87.5	49.9
	7	N	278.6	54.0
	8	N	273.0	61.4
	9	O	92.3	22.6
	10	O	338.8	27.5
	11	O	124.4	20.3
	12	N	275.5	72.6
	13	O	96.6	52.6
	14	O	144.8	31.3
	15	N	159.9	52.0
	16	S	154.3	54.8
	17	O	186.7	53.7
	18	F	264.5	50.4
	19	V	259.9	90.0
3-6	1	N	229.7	68.3
	2	N	234.5	56.7
	3	F	219.7	63.6
	4	N	21.9	75.4
	5	O	324.9	33.6
	6	O	15.3	33.9
	7	O	250.1	43.1
	8	N	116.5	27.6
	9	S	121.7	32.5
	10	L	216.9	57.1
	11	O	137.4	39.2
	12	L	240.1	66.6
	13	O	133.6	36.7
	14	O	105.4	19.8
	15	O	105.8	19.8
	16	N	211.4	63.4
	17	N	257.0	28.4
	18	O	351.5	33.0
	19	N	342.5	28.4
	20	N	353.5	17.1
	21	N	335.0	26.5
	22	F	258.2	47.1
	23	L	189.8	44.5
	24	O	239.4	30.4

Table 9 Continued.

	25	O	114.0	24.1
	26	O	132.4	31.5
	27	S	127.8	32.9
	28	O	128.7	61.0
	29	F	164.3	51.8
	30	L	189.9	45.9
	31	L	183.2	46.9
	32	O	25.8	21.2
	33	O	48.9	24.6
	34	L	227.1	38.3
	35	O	193.2	53.7
	36	L	184.9	8.6
	37	O	231.4	44.7
	38	V	131.9	76.3
7-9	1	V	120.6	63.6
	2	N	174.1	58.1
	3	N	184.5	66.6
	4	F	72.1	41.0
	5	L	264.1	40.6
	6	N	42.1	49.6
	7	N	221.3	64.5
	8	F	82.4	47.9
	9	N	108.8	55.3
	10	O	55.1	25.3
	11	V	97.8	69.8
	12	V	159.2	56.9
	13	V	36.1	84.2
	14	O	302.8	46.7
	15	N	144.0	61.5
	16	N	167.8	80.3
	17	V	34.1	90.0

APPENDIX 4

1:1 MAPS OF SEDIMENTARY SPOT CORE

WITH BEST FIT SINUSOIDS

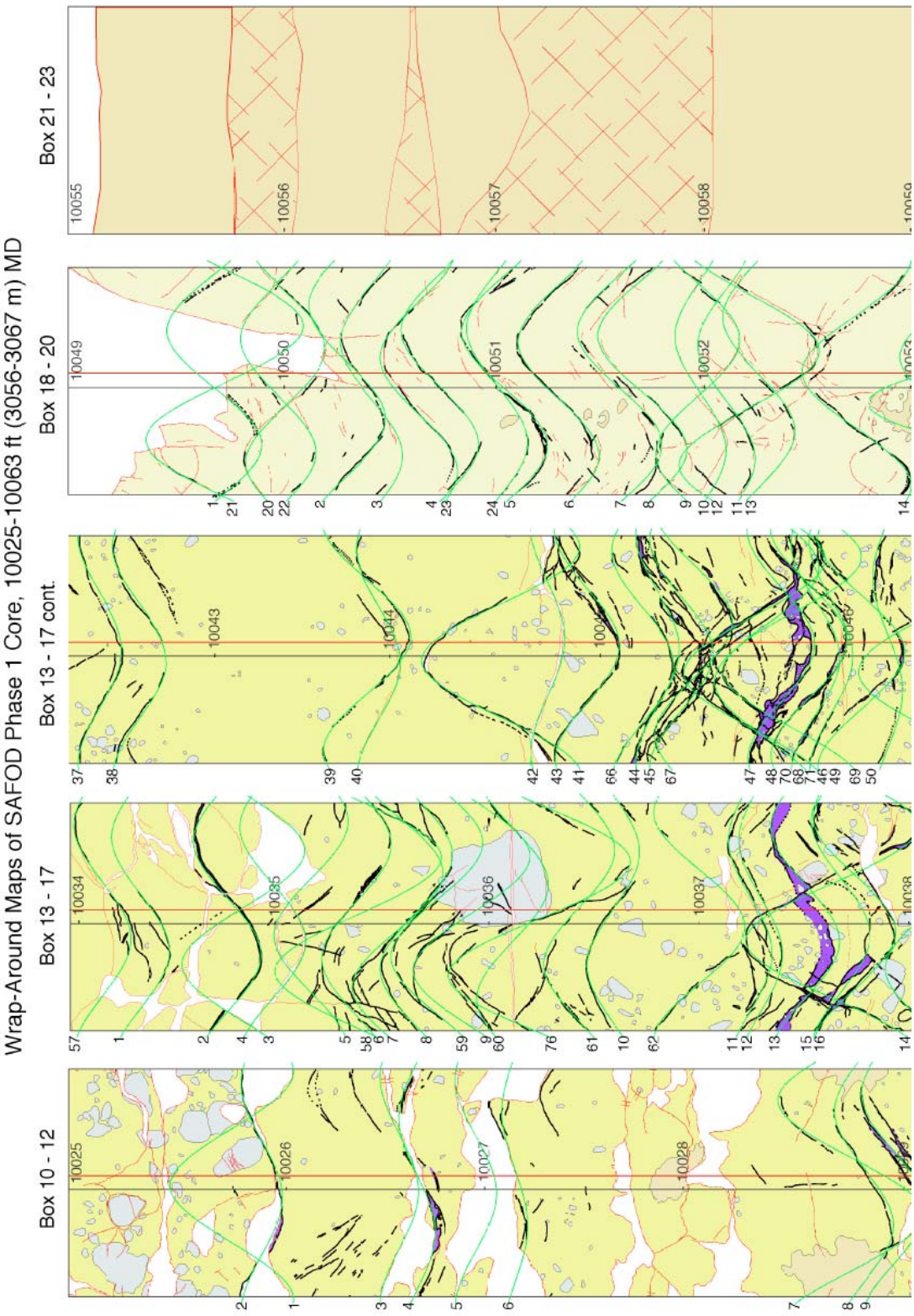

Figure 20. 1:1 maps of sedimentary spot core showing sinusoid fits to each planar feature (Table 10).

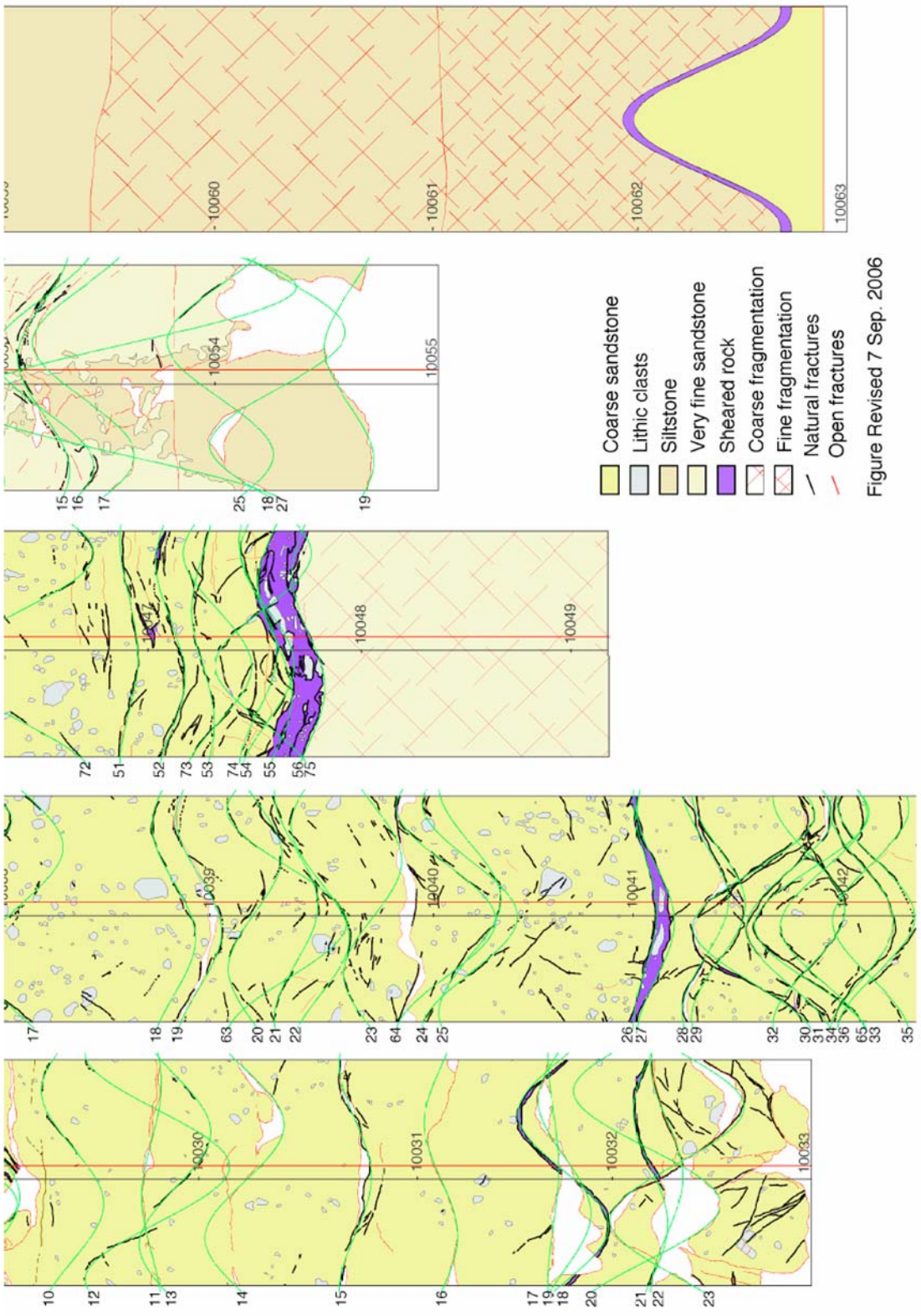

Figure 20. Continued.

Table 10. Orientation of all features noted on sedimentary spot core with respect to geographic North

Box Number	Sinusoid Number	Feature	Strike	Dip
10-12	1	O	63.9	59.8
	2	N	264.1	29.8
	3	O	254.3	28.1
	4	S	319.4	26.9
	5	O	257.5	29.9
	6	N	309.1	19.7
	7	N	290.5	63.7
	8	N	307.9	39.5
	9	S	279.8	41.8
	10	N	290.7	41.0
	11	O	098.5	15.5
	12	N	230.5	63.7
	13	N	174.9	45.0
	14	O	164.3	47.9
	15	N	247.9	24.1
	16	O	342.2	25.0
	17	O	233.5	8.5
	18	S	327.5	51.7
	19	O	305.9	36.4
	20	O	291.0	64.1
	21	S	323.1	25.6
	22	N	248.0	24.1
	23	N	135.8	61.9
13-17	1	N	314.3	38.8
	2	N	320.2	43.1
	3	O	154.3	59.6
	4	O	298.2	42.5
	5	O	108.1	45.8
	6	N	144.6	43.9
	7	N	190.1	51.5
	8	N	161.6	45.1
	9	N	163.1	58.3
	10	N	156.4	36.0
	11	N	318.4	31.3
	12	N	319.4	31.3
	13	S	298.8	43.6
	14	N	116.4	67.3
	15	N	277.5	39.3
	16	N	283.7	49.0
	17	N	160.8	49.2
	18	N	307.3	31.3
	19	N	296.1	32.5
	20	N	171.0	36.7

Table 10 Continued.

21	N	254.7	31.3
22	N	306.7	39.1
23	N	182.6	39.1
24	N	272.1	53.1
25	N	244.6	41.0
26	S	265.6	18.0
27	N	280.7	27.5
28	N	245.7	32.8
29	N	253.1	36.8
30	N	107.8	59.7
31	N	108.8	50.5
32	N	262.7	44.8
33	N	105.3	58.0
34	N	280.7	41.9
35	N	097.6	46.9
36	N	272.7	47.1
37	N	260.2	31.3
38	N	277.3	36.5
39	N	239.1	50.6
40	N	280.1	31.3
41	N	096.5	65.6
42	O	242.0	25.4
43	N	252.6	41.9
44	N	258.0	31.3
45	N	265.9	41.3
46	N	116.0	63.0
47	S	251.5	42.9
48	N	246.3	46.6
49	N	263.9	50.3
50	N	326.3	22.0
51	N	276.4	14.6
52	N	311.3	22.1
53	N	027.8	17.0
54	N	294.0	36.8
55	N	343.8	25.1
56	S	330.7	25.1
57	N	294.9	38.5
58	N	164.8	66.6
59	N	141.3	51.9
60	N	207.9	44.8
61	N	153.0	44.5
62	N	275.2	51.7
63	N	281.8	59.1
64	N	276.6	54.3
65	N	105.3	50.1

Table 10 Continued.

	66	N	271.4	40.6
	67	N	214.5	47.0
	68	N	129.5	55.5
	69	N	111.2	62.6
	70	N	272.2	33.9
	71	N	270.4	30.9
	72	N	113.8	63.1
	73	N	296.1	43.3
	74	N	276.6	27.7
	75	N	113.8	53.5
	76	N	171.2	68.4
18-20	1	N	274.9	52.5
	2	N	121.8	47.9
	3	N	292.6	40.7
	4	N	317.8	45.3
	5	N	276.9	49.9
	6	N	292.4	48.6
	7	N	276.1	49.3
	8	N	282.7	50.9
	9	N	107.8	49.4
	10	O	283.7	35.0
	11	N	297.2	38.9
	12	N	125.8	62.8
	13	N	253.3	45.3
	14	N	339.9	56.5
	15	N	323.5	35.6
	16	N	300.6	54.2
	17	N	298.3	54.9
	18	O	100.6	62.2
	19	O	307.0	34.8
	20	N	233.8	47.1
	21	N	086.0	65.4
	22	N	287.2	46.3
	23	N	273.9	47.1
	24	N	271.5	39.9
	25	N	295.6	55.9
	26	N	317.0	58.5
	27	B	039.4	77.8

VITA

Name:	Rafael Almeida
Address:	801 Cleveland St. #3309, Houston, TX, 77019
Email Address:	ralmeida24@gmail.com
Education:	B.S., Geological Engineering, Universidad de Los Andes – Venezuela 2004
	M.S., Geology, Texas A&M University, 2007